Electrostatic effects on ligand-assisted transfer of metals to (bio)accumulating interfaces and metal complexes (bioavai)lability

Jerome F. L. Duval, Herman P. Van Leeuwen, Raewyn M. Town

Graphical Abstract

Electrostatic effects on ligand-assisted transfer of metals to (bio)accumulating interfaces and metal complexes (bioavai)lability.

Jérôme F. L. Duval [a,*], Herman P. van Leeuwen [b,c], Raewyn M. Town [c]

[a] Université de Lorraine, CNRS, LIEC, F-54000 Nancy, France.
[b] Physical Chemistry and Soft Matter, Wageningen University & Research, Stippeneng 4, 6708 WE Wageningen, The Netherlands.
[c] ECOSPHERE, Department of Biology, Universiteit Antwerpen, Groenenborgerlaan 171, 2020 Antwerpen, Belgium.
* Corresponding author: jerome.duval@univ-lorraine.fr

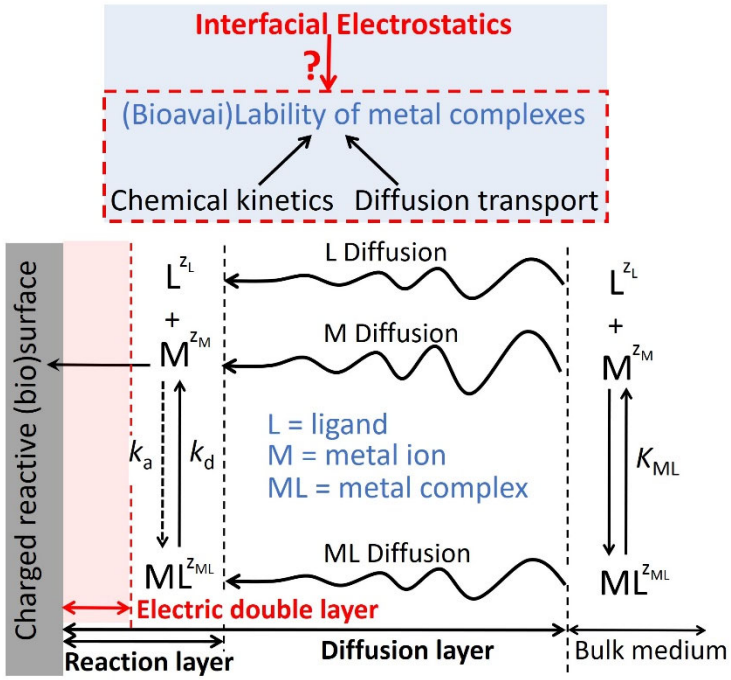

Electrostatic effects on ligand-assisted transfer of metals to (bio)accumulating interfaces and metal complexes (bioavai)lability.

Jérôme F. L. Duval [a,*], Herman P. van Leeuwen [b,c], Raewyn M. Town [c]

[a] Université de Lorraine, CNRS, LIEC, F-54000 Nancy, France.
[b] Physical Chemistry and Soft Matter, Wageningen University & Research, Stippeneng 4, 6708 WE Wageningen, The Netherlands
[c] ECOSPHERE, Department of Biology, Universiteit Antwerpen, Groenenborgerlaan 171, 2020 Antwerpen, Belgium
* Corresponding author: jerome.duval@univ-lorraine.fr

Abstract.

The electric charge at a reactive interface influences the diffusion rate of ionic species towards the interface as well as their local concentration profiles. For metal ions (M) and their complexes (ML) formed with ligands (L), the interfacial electric field at a metal-consuming interface will lead to coupling between reaction layer and electric Debye layer, interfacial polarization of species concentrations and, thereby, so-far unexplored changes in ML contribution (lability) to sustain or not metal accumulation fluxes. A formalism and computational approach -based on coupled steady-state Nernst-Planck equations corrected for interfacial electrostatics and chemical kinetics- are here elaborated to obtain relevant metal surface flux and spatial distributions of M, L and ML. ML lability is subsequently derived and evaluated for practical settings of ML chemodynamics and macrosurface electrostatics under metal sink boundary condition. The extent to which the interfacial electric field affects lability of metal complexes depends on the charges of the reactive species and macrosurface. For example, repulsive M/ML-macrosurface interactions lead to significant loss of lability. Mass transfer features of ligands, even when present in large excess in bulk solution, are also found to impact on lability, even for moderately charged reactive surfaces. Predictions are in qualitative agreement with the available experimental data.

Keywords: Colloid electrostatics, metal, ion reactive transfer, lability, reaction layer, Koutecký-Koryta, electric double layer, metal bioaccumulation, theory, bioavailability.

1. Introduction.

In aqueous environmental media, metals (and other elements) typically exist in several different physicochemical forms, i.e. chemical species. The various chemical species differ in their chemical reactivity which influences their fate, transport, impact on biota (e.g. toxicity) and/or bioaccumulation. For example, free metal ions, $M(H_2O)_x^{n+}$, are generally bioavailable for organisms, whereas the bioavailability of metals in complexed forms, hereafter termed as ML with L a metal binding ligand, typically depends on the extent to which free M can be released from ML over the timescale of the biouptake process [1]. The distribution (or speciation) of chemical species present in a medium of given physicochemical composition is determined by both the thermodynamic and kinetic properties of the system. Relevant parameters include stability constants for ligand protonation, K_{HL}, and metal complexation, K_{ML}, rate constants for metal complex association, k_a, and dissociation, k_d, as well as the diffusion coefficients for the free metal ion, D_M, the free ligand, D_L, and the metal complex, D_{ML}. Concepts have been developed for describing the dynamics of chemical speciation in aqueous media [1]. Under typical practical conditions met for trace metals, the concentration of complexing ligand L is sufficiently higher than that of the metal ion such that the association reaction between M and L is quasi-monomolecular. In such case, the concentration of free L in the bulk medium, c_L^*, is effectively constant and can be subsumed in the association rate constant, k_a, by writing $k_a^' = k_a c_L^*$. A first consideration is whether the system is sufficiently *dynamic* for bulk equilibrium between M and ML to be maintained within a given timescale, *t*. At the level of the volume reaction in bulk solution, discrimination is made between dynamic and inert complexes on the basis of the characteristic lifetimes of the free M (given by $1/k_a^'$) and ML ($1/k_d$) relative to *t*. That is, ML is dynamic, and there is then frequent interchange between M and ML, if [1]:

$$k_a^' t >> 1 \text{ and } k_d t >> 1 \quad (1)$$

and ML is inert if:

$$k_a^' t << 1 \text{ and } k_d t << 1 \quad (2)$$

In the context of surface reactivity, i.e. an ongoing interfacial process which consumes free M (or another physicochemical form) at a given surface, additional criteria are involved to assess the kinetic features of the system. Taking the example of an organism that accumulates free M, the biouptake process will perturb local equilibria involving M and, in turn, induce a chain of reactions shown schematically in **Figure 1**. The local concentration of free M on the medium side of the organism/medium interface is decreased, thereby provoking dissociation of the complexed forms ML. If free M is the only reactive (i.e. uptaken) species as considered in the example, the extent to which complexed forms of M contribute to the interfacial biouptake of M depends on the interplay between the rate of M bioaccumulation, the dissociation rate of ML, and the (coupled) rates of diffusion of M and ML. Two limiting cases can then be identified. At one extreme, if the rate of interfacial biouptake is much slower than the rate at which free M can diffuse towards the interface, then the local concentration of free M remains practically constant, the local equilibrium between M and ML

is effectively not perturbed, and the rate of the interfacial process will be proportional to the equilibrium concentration of free M in the bulk aqueous medium. At the other extreme, if the interfacial process is faster than the diffusive supply flux of free M, then a concentration gradient of free M will be established at the interface. In such a situation, ML will dissociate to the full extent possible to buffer the local free M concentration, thereby also generating a concentration gradient in ML at the interface.

Consideration of all the involved timescales is therefore fundamental for a proper interpretation of the dynamics of ongoing interfacial processes. For example, in the domain of metal bioavailability to organisms, the widely used biotic ligand model (BLM) and free ion activity model (FIAM) assume a priori that the equilibrium concentration of free M in the bulk solution is the only relevant parameter irrespective of timescales of all possibly contributing processes [2]. However, such assumptions correspond to a limiting scenario of the overall dynamic speciation/biouptake framework. Compliance with the underlying kinetic criteria is thus a fundamental prerequisite for valid application of equilibrium-based models. As a support of such a requirement, there are many practical examples illustrating the failure of BLM and FIAM to interpret metal biouptake data on e.g. freshwater algae [3,4] or plants [5,6]. Whereas the example above is given for metal bioaccumulating interfaces, other surface reactivity processes where coupling between diffusion and chemical kinetics must be considered include e.g. surface adsorption of aqueous analytes or gas molecules [7], redox reactions at metallic surfaces [8], infection of biological cells by viruses [9], and particle-assisted delivery of drugs [10].

The concept of lability is invoked to describe the extent to which ML can maintain equilibrium with free M in the context of an ongoing interfacial process that consumes free M [1]. The two extremes of "labile" and "inert" complexes are readily identified by comparing the limiting kinetic flux controlled by finite ML dissociation rates to the limiting diffusive flux [11]. Specifically, a lability parameter, $\mathcal{L}$, is defined as the ratio of the kinetic flux originating from dissociation of ML, J_{kin}, and the (coupled) diffusive flux of M and ML towards the interface, J_{dif}:

$$\mathcal{L} = J_{kin} / J_{dif} \tag{3}$$

When $\mathcal{L}$ >> 1, ML is fully labile and there is coupled diffusion and frequent interconversion of M and ML during their transport through the diffusion layer to the reactive surface (e.g. an organism or an electrode). That is, even when the reactive surface acts as a perfect sink for free M (i.e. the concentration of free M at the medium side of the interface, c_M^a, approaches zero), ML maintains equilibrium with free M over all spatial and timescales. In such case the maximal J_{dif} is given by:

$$J_{dif} = \overline{D} c_{M,t}^* (1/\overline{\delta} + 1/a) \qquad [\text{mol m}^{-2}\ \text{s}^{-1}] \tag{4}$$

where $c_{M,t}^*$ is the total metal concentration (mol m^{-3}) in the bulk solution (including free and complexed metal forms), $\overline{D} = \sum_{i=M,ML} D_i c_i^* / c_{M,t}^*$ is the mean diffusion coefficient of free M and ML (m^2 s^{-1}), $\overline{\delta}$ is the mean diffusion layer thickness (m) arising from the coupled diffusion of M and ML, and a is the radius of the consuming

interface (in spherical case). At a macroscopic surface, planar diffusion prevails and hydrodynamic conditions govern $\overline{\delta}$ [12]. At micro- and nano-scale surfaces, radial diffusion dominates and a then corresponds to the diffusion layer thickness [1]. Eq. (4) thus defines the flux of free M species at the surface of a metal-accumulating (bio)particle in the case where the metal complex ML is fully labile. Accordingly, the expression of this flux involves only the diffusion coefficients of M and ML weighted by the bulk concentrations of M and ML, and the thickness of the diffusion layer operational at the (bio)particle/medium interface corrected or not by hydrodynamics depending on whether planar or spherical diffusion prevails. The reader is referred to [1] (and references therein) for further details on the derivation of Eq. (4). At the other extreme, when $\mathcal{L}$ << 1, ML is nonlabile and its contribution to the flux of M corresponds to the kinetically controlled limit, J_{kin}. The Koutecký-Koryta approximation provides a useful means to compute the magnitude of J_{kin} [13-15]. In brief, the diffusion layer is divided into a labile and a nonlabile region, and within the nonlabile region (the so-called ***reaction layer***) the contribution of ML to the flux of M is purely kinetic. The thickness of the reaction layer is generally determined by the mobility of free M, D_M, and its mean free lifetime ($1/k_a c_L^*$) together with the mobility of the complex (D_{ML}) and its mean free lifetime ($1/k_d$). In the here-considered case of molecular ligands, the reaction layer thickness, hereafter denoted as μ_o, is generally given by [1,16]:

$$\mu_o = \left(k_a c_L^* / D_M\right)^{-1/2} \quad \text{[m]} \quad (5)$$

The expression for J_{kin} follows as:

$$J_{kin} = k_d c_{ML}^* \mu_o \quad \text{[mol m}^{-2}\text{ s}^{-1}\text{]} \quad (6)$$

We highlight that as soon as a concentration gradient is established at an interface, i.e. $c_M^a < c_M^*$, the potential for ML species to dissociate and contribute to the flux of free M must be considered. That is, even if the overall process appears to be controlled by the concentration of free M in the bulk solution, underlying buffering of the free M concentration by the dissociation of ML can be crucial [17-20].

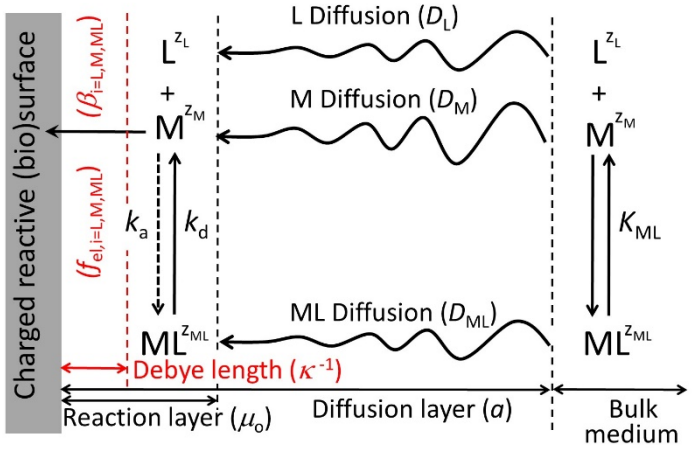

Figure 1. Schematic representation of the transport, chemical kinetic and electrostatic contributions to the overall flux of metal ions (M) at an electrically charged interface (e.g. organism or electrode) that consumes free M. The valences of species M, ML and L are denoted as z_M, z_{ML} and z_L, respectively, and the diffusion layer thickness is set to a, the curvature radius of the consuming interface. The work aims at addressing the effects of electrostatics on the lability of ML complex and, therewith, the way the interplay between reaction layer, electric double layer and diffusion layer affects the overall transfer of M to the reactive surface. The electrostatic factors $\beta_{i=L,M,ML}$ and $f_{el,i=L,M,ML}$ refer to the Boltzmann accumulation/depletion and conductive acceleration/retardation of diffusion for L, M and ML species, respectively. See text for details.

In aqueous environmental media, most abiotic and biotic surfaces carry a net charge, the sign and magnitude of which depend on the functional groups present, their (de)protonation constants, as well as the prevailing pH and ionic strength of the aqueous medium. The presence of charged sites gives rise to an electric field around and within the material. The magnitude and nature of such electric fields can be experimentally determined by electrokinetics and surface conductivity measurements [21,22] that we shall not detail here. In the case of ideal hard surfaces which are impermeable to ions and fluid flow, Smoluchowski theory can be used to estimate zeta potentials from electrophoretic and surface conductivity data [22-25]. The approach has been successfully applied to describe the influence of ion sorption on the electrokinetic features of impermeable thin fluoropolymer films [26] and clay minerals [27]. In the case of soft interfaces (i.e. permeable to ions and/or fluid flow), theory is available to account for the 3D distributions of their structural charges as well as their permeability to ions and/or flow [28,29] (and references therein). Such concepts have elucidated the electrostatic, hydrodynamic and structural features of a range of planar and spherical systems including nanometer thick polyelectrolyte films and polymer brushes [29-32] and microbes like bacteria and viruses [33-37].

An interfacial electric field invokes attraction or repulsion of ions, which will modify the local concentration profiles of charged species in the surrounding medium. This effect of the electric field comes on top of the chemical reactivity considerations elaborated above. The *interplay* between the electric field and chemical processes will determine the overall reactivity profile of the system. For example, in the case of metal ion association with charged soft nanoparticulate complexants, discrimination between electrostatic and intrinsic chemical reactivity is fundamental for a proper description of the thermodynamic and kinetic features of the metal complexes [38,39]. Also, in the case of biota, the electrostatic features of bacteria evaluated from electrophoresis measurements and application of soft surface electrokinetic concepts have been shown to play a role in determining homo-aggregation, adhesion, and biofilm formation [40] as well as interactions with metal ions [34,41] and nanoparticles [42]. Furthermore, in the case of SARS-CoV-2 variants, the electric field of the virions seems to play an important role in determining their environmental reactivity (e.g. sorption on airborne particulate matter) and biological reactivity (transfer rate to ACE2 receptors of alveolar tissues, as well as their strength of association with ACE2 receptors and antibodies) [43-45]. In most environmentally and biologically relevant cases, the magnitude (and sign) of the net charge depends on the pH, ionic strength and electrolyte composition of the surrounding medium. Large differences in the nature and magnitude of interfacial electric fields are thus expected along salinity gradients, e.g. from freshwaters with few millimolar electrolyte concentration to marine systems comprising of the order of 1 molar electrolyte.

Given the above elements, we focus here on how the presence of an electric field at a reactive surface/medium interface influences the lability of metal complex species in the context of an ongoing metal (bio)accumulating process (**Figure 1**). Despite the evident fundamental importance of electric fields on chemical reactivity in interfacial zones, there is thus far no rigorous theory available to describe such systems.

Quantitative description of the involved processes requires coupling of length and time scales that has not been realized yet, i.e. electric double layer versus reaction layer versus diffusion layer thicknesses, and their interrelated spatial and time dependencies. The conceptual framework elaborated here connects the effects of electrostatic fields at environmentally and biologically relevant surfaces with the chemical interactions between M, ML and L species and with the resulting contribution of ML to the supply flux of free M towards the M-consuming interfaces. The formalism includes explicitly the governing ligand L-(bio)surface, metal M-(bio)surface, complex ML-(bio)surface electrostatic interactions while those between M and L in the surrounding medium are subsumed in the pertaining ML formation/dissociation kinetic and stability constants. The analysis is performed under perfect sink conditions thereby providing an estimate of the maximal ML contribution to the M supply flux as a function of the relevant electrostatic descriptors of the reactive surface.

2. Theory.

2.1. Formulation of the problem, concentration profiles of metal species, and lability of metal complexes.

Setting the stage. In the following, we consider the reactive transfer of metal ions M^{z_M} with valence z_M from a bulk medium containing a metal-complexing ligand L, to a charge metal-consuming interface of spherical geometry with radius of curvature *a* (**Figure 1**). Typical values of *a* are here of the order of 1 to 10 μm, in line with usual dimensions of microorganisms or microelectrodes. In the bulk medium far from the interface, the equilibrium between M, ML complex and L, with valence $z_{i=M,L,ML}$, is maintained so that their bulk concentrations denoted as $c^*_{i=M,L,ML}$ satisfy $c^*_{ML} / c^*_M c^*_L = K_{ML}$. The overall scheme of M transfer involves the diffusion of M, L and ML, with diffusion coefficients $D_{i=M,L,ML}$, and the interconversion kinetics between M and ML with association and dissociation kinetic constants k_a and k_d, respectively, connected to K_{ML} via $K_{ML} = k_a / k_d$. Expression of k_a for the here-considered molecular ligands L follows Eigen-Fuoss theory [1,46,47] and involves the electrostatic contribution stemming from Coulombic interactions between M and L. For the sake of convenience, we introduce the dimensionless ML stability constant $\bar{K}_{ML}$ defined by $\bar{K}_{ML} = K_{ML} c^*_L$ and the diffusion coefficients ratio $\varepsilon = D_{ML} / D_M$. In line with conditions prevailing in natural media where metals are present in trace concentrations, the medium contains here an indifferent background electrolyte of bulk concentration c^∞ in large excess over M, i.e. $c^\infty >> c^*_M$. Following previous reports [48-50], the M-consuming particle of radius *a* is positioned in a Kuwabara unit cell with radius r_c such that the particle volume/solution ratio, ϕ, in that cell equates with the one prevailing in the entire medium, i.e. $\phi = (a / r_c)^3$. We further consider steady-state transport of M which is rapidly achieved for accumulating spherical nano/microparticles, i.e. the transient regime required for building the interfacial M/ML diffusion layer is ignored [48-50]. In addition, the practical situation of diluted particle dispersions is treated, i.e. $\phi << 1$ or $r_c >> a$. Under such conditions, there is no overlap between diffusion/reaction layers of neighboring particles,

the electric field at the particle/medium interface is at equilibrium, and the associated electric double layer is fully relaxed [48,49]. The use of a (Kuwabara) cell model for practical situations where $\phi << 1$ is generally required because such a model helps to formulate the kinetics of metal depletion from bulk solution. Such a depletion process can indeed occur in the course of metal (bio)accumulation by the (bio)particles dispersed in the medium depending on a number of factors, e.g. concentrations of (bio)particles (i.e. ϕ) and metal species, and magnitudes of the thermodynamic and kinetic descriptors of metal complexation and (bio)accumulation. The benefits of such a Kuwabara cell model in this context have been illustrated in previous reports [48,49]. Even though bulk metal depletion is not considered in the current study where the focus is given on the electrostatic determinants of metal (bioavai)lability, we formulate the problem below with use of a Kuwabara cell model because of its genericity. Some of the theoretical expressions derived in this work as a function of ϕ (or r_c) will be further used in a forthcoming manuscript for a quantitative interpretation of the bioluminescence response of metal-detecting whole cell bacterial sensors [41] under metal depletive conditions. Considering a *z*:*z* symmetrical background electrolyte, the Debye layer thickness is defined by $\kappa^{-1} = \left(2z^2F^2c^\infty / RT\varepsilon_o\varepsilon_r\right)^{-1/2}$, with *F* the Faraday, *R* the gas constant, *T* the absolute temperature and $\varepsilon_o\varepsilon_r$ the dielectric permittivity of the medium.

Metal species concentration profiles, electrostatics. Adopting radial coordinate r with the origin $r = 0$ at the center of the M-consuming spherical (bio)particle, the spatial distributions of the M, L and ML concentrations, denoted as $c_{i=M,L,ML}(r)$, are then governed by the coupled steady-state Nernst-Planck equations corrected for electrostatic and chemical kinetic terms, i.e.

$$\begin{cases} D_M\nabla_r^2 c_M(r) + k_d c_{ML}(r) - k_a c_{ML}(r)c_L(r) + z^{-1}z_M D_M\left\{c_M(r)\nabla_r^2 y(r) + \left[\left(\mathrm{d}y(r)/\mathrm{d}r\right)\left(\mathrm{d}c_M(r)/\mathrm{d}r\right)\right]\right\} = 0 \quad \text{(a)} \\ D_{ML}\nabla_r^2 c_{ML}(r) - k_d c_{ML}(r) + k_a c_{ML}(r)c_L(r) + z^{-1}z_{ML}D_{ML}\left\{c_{ML}(r)\nabla_r^2 y(r) + \left[\left(\mathrm{d}y(r)/\mathrm{d}r\right)\left(\mathrm{d}c_{ML}(r)/\mathrm{d}r\right)\right]\right\} = 0 \quad \text{(b)} \\ D_L\nabla_r^2 c_L(r) + k_d c_{ML}(r) - k_a c_M(r)c_L(r) + z^{-1}z_L D_L\left\{c_L(r)\nabla_r^2 y(r) + \left[\left(\mathrm{d}y(r)/\mathrm{d}r\right)\left(\mathrm{d}c_L(r)/\mathrm{d}r\right)\right]\right\} = 0 \quad \text{(c)} \end{cases} \tag{7}$$

where $\nabla_r^2 f \equiv r^{-2}\mathrm{d}\left(r^2\mathrm{d}f/\mathrm{d}r\right)/\mathrm{d}r$ is the Laplacian operator in spherical geometry with f a dummy function of the radial position *r*, and $y(r)$ is the dimensionless interfacial electrostatic potential at position *r* defined by $y(r) = zF\psi(r)/RT$ with $\psi(r)$ the corresponding potential. In Eq. (7), the first term corresponds to the diffusion of M, ML or L (Eq. (7a), (7b) and (7c), respectively), the second and third terms refer to the rates of apparition and consumption of M, ML and L as a result of the formation and dissociation of the ML complex, and the last term between brackets originates from the effect of the interfacial electrostatic field on the spatial distributions of M, ML or L concentration from the (bio)particle surface to the electroneutral bulk medium. As argued in the Introduction, media of practical interest are defined by an excess of L over M so that the spatial concentration profile $c_L(r)$ is not significantly impacted by the M complexation process. Accordingly, dropping the $k_{a,d}$-dependent terms in Eq. (7c) and solving for the resulting equation leads to $c_L(r) = c_L^*\beta_L(r)$, which is nothing else than the equilibrium L concentration profile, $c_L^{(e)}(r)$, involving the

classical Boltzmann factor defined by $\beta_L(r)=e^{-z_L y(r)/z}$. Substituting this expression of $c_L(r)$ in Eqs. (7a)-(7b), we then obtain

$$\begin{cases} Y''(\bar{r})+z^{-1}z_M\left\{Y(\bar{r})\Omega(\bar{r})+y'(\bar{r})Y'(\bar{r})+\varepsilon\bar{K}_{ML}\left(z_M^{-1}z_{ML}-1\right)\left[\omega_{ML}(\bar{r})\Omega(\bar{r})+\omega_{ML}'(\bar{r})y'(\bar{r})\right]\right\}=0 & \text{(a)} \\ \omega_{ML}''(\bar{r})-\omega_{ML}(\bar{r})\left\{\dfrac{1+\varepsilon\bar{K}_{ML}}{\varepsilon\bar{K}_{ML}}\bar{\kappa}_a\beta_L(\bar{r})-z^{-1}z_{ML}\Omega(\bar{r})\right\}+z^{-1}z_{ML}\omega_{ML}'(\bar{r})y'(\bar{r})+\dfrac{\bar{\kappa}_a}{\varepsilon\bar{K}_{ML}}\beta_L(\bar{r})Y(\bar{r})=0 & \text{(b)} \end{cases} \quad (8)$$

where we have introduced the dimensionless space scale $\bar{r}=r/a-1$, the change in variables $\omega_{i=M,ML}(r)=r\,\bar{c}_i(r)$ (m) with $\bar{c}_{i=M,ML}(r)=c_i(r)/c_i^*$ (dimensionless), and the radial function $Y(r)$ (m) defined by linear combination of $\omega_{i=M,ML}(r)$ according to $Y(r)=\omega_M+\varepsilon\bar{K}_{ML}\omega_{ML}$. The symbols ' and '' correspond to the first and second derivative with respect to $\bar{r}$, respectively, and this nomenclature applies in the developments below. The radial function $\Omega(\bar{r})$ in Eq. (8) depends on particle electrostatics according to $\Omega(\bar{r})=y''(\bar{r})+(1+\bar{r})^{-1}y'(\bar{r})$. Eq. (8) further involves the key Damköhler number $\bar{\kappa}_a=D_M^{-1}k_a c_L^* a^2$ that can be seen as a dimensionless ML formation rate constant that compares the diffusional timescale $D_M^{-1}a^2$ with the reaction timescale $1/k_a c_L^*$. Equivalently, $\bar{\kappa}_a^{1/2}$ compares *a* with the reaction layer thickness μ_o defined by Eq. (5) in the absence of electrostatic effects. The fluxes of M and ML at any position *r* in the vicinity of the microparticle, denoted as $J_{i=M,ML}(r)$, include diffusion and conduction contributions according to

$$J_{i=M,ML}(r)=D_i\left(dc_i(r)/dr+z^{-1}z_i c_i(r)dy(r)/dr\right)=\frac{J_i^o}{a(1+\bar{r})}\left(\omega_i'(\bar{r})-\omega_i(\bar{r})\left[(1+\bar{r})^{-1}-z^{-1}z_i y'(\bar{r})\right]\right) \quad (9)$$

where $J_{i=M,ML}^o=D_i c_i^*/a$ are the maximal M and ML diffusion fluxes. The solution of Eq. (8) defines the searched concentration profiles $c_{i=M,ML}(r)$ after formulation of the required boundaries for $\omega_{i=M,ML}$ and Y. A first set of boundaries applies at the particle surface and specifies (i) the sink condition considered for M (i.e. $c_M(r=a)=0$), and (ii) the non-accumulation of ML complex at the reactive surface, i.e. $J_{ML}(r=a)=0$. In terms of $\bar{r}$, ω_{ML} and Y, these conditions translate into

$$\begin{cases} Y(\bar{r}=0)=\varepsilon\bar{K}_{ML}\omega_{ML}(\bar{r}=0) & \text{(a)} \\ \omega_{ML}'(\bar{r}=0)=\omega_{ML}(\bar{r}=0)\left(1-z^{-1}z_{ML}y'(\bar{r}=0)\right) & \text{(b)} \end{cases} \quad (10)$$

The second set of boundaries associated to Eq. (8) holds in the bulk medium ($r=r_c$) and imposes bulk concentration values for $c_{i=M,ML}$, i.e.

$$\begin{cases} Y(\bar{r}=\bar{r}_c)/r_c=\left(1+\varepsilon\bar{K}_{ML}\right) & \text{(a)} \\ \omega_{ML}(\bar{r}=\bar{r}_c)/r_c=1 & \text{(b)} \end{cases} \quad (11)$$

with $\bar{r}_c=r_c/a-1$. Eqs. (8)-(11) are valid irrespectively of the expression $y(r)$ chosen for the electrostatic potential profile at the particle/medium interface. As the particle radius *a* is of the order of the micron or larger, it well exceeds the Debye layer thickness under practical salinity conditions (i.e. κ^{-1}~0.3-10 nm for $1\text{ mM}\le c^\infty\le 1\text{ M}$). In turn, the spatial distribution of the potential is determined by the non-linearized Poisson-

Boltzmann (PB) equation written here in planar symmetry ($\kappa a >> 1$). For the radial domain of interest $a \le r \le r_c$, the exact solution of the planar PB equation reads [51]

$$y(r) = \ln\left[\frac{1+\mathrm{e}^{-\kappa(r-a)}\tanh(y_a/4)}{1-\mathrm{e}^{-\kappa(r-a)}\tanh(y_a/4)}\right]^2 \tag{12}$$

where $y_a = y(r=a)$ is the scaled particle surface potential. For a poorly to moderately charged particle, i.e. $|y_a| << 4$, Eq. (12) reduces to the well-known Debye-Hückel result

$$y(r) = y_a \mathrm{e}^{-\kappa(r-a)} \tag{13}$$

Lability parameter. The formulation of the lability parameter $\mathcal{L}$ according to Eq. (3) requires knowledge of the expression of the diffusion flux J_{dif} and the kinetic flux J_{kin}. The derivation of the expression of J_{kin} is made possible by invoking the Koutecký-Koryta (KK) approximation and the reaction layer concept which to date has been formulated without accounting for electrostatic effects. Under such conditions, a far-reaching equivalence between lability outcomes derived from the KK approximation and from the exact solution of the relevant M and ML chemical kinetics-diffusion equations was demonstrated by van Leeuwen et al. [52]. These authors also extended the KK approximation to the partially labile regime by computing J_{kin} on the basis of the concentration of ML within the reaction layer, rather than that in the bulk solution. This concept was further elaborated by Galceran et al. [53] who showed that the degree of ML complex lability, hereafter denoted as ξ with $0 \le \xi \le 1$, could be evaluated from the deviation of the ML surface concentration from bulk concentration value. It is stressed that an elaborated evaluation of ML lability via the lability index ξ is required to get information on the nuances of lability beyond the extremes of labile versus inert metal complexes as captured by the lability parameter $\mathcal{L}$ defined by Eq. (3). Accordingly, the situation $c_{ML}(r=a) = c_{ML}^*$ holds for inert ML complexes with $\xi = 0$, and this limit basically corresponds to that assumed a priori in BLM and FIAM. In the other extreme of fully labile complexes ($\xi = 1$), M-ML equilibrium is maintained everywhere at all times within the diffusion layer, including at the particle surface, and the resulting equality $c_{ML}(r=a) = 0$ then defines labile ML under the here-adopted sink condition for M. Extending this idea by Galceran et al. [53] to the situation where electrostatics effects are operational, the expression for the lability index ξ becomes

$$\xi = 1 - c_{ML}(r=a) / \left(c_{ML}^* \beta_{ML}(r=a)\right) \tag{14}$$

where $\beta_{ML}(r=a) = \mathrm{e}^{-z_{ML} y_a / z}$ is the ML equilibrium Boltzmann factor at the particle surface, and $c_{ML}(r=a)$ in Eq. (14) is inferred from the solution of Eqs. (8)-(12) obtained as briefly outlined below.

Numerical analysis. For given descriptors of interfacial electrostatics (y_a and $1/\kappa$) and prescribed values of particle radius and concentration (a, ϕ or r_c), of M-ML interconversion kinetic constants ($k_{a,d}$), ML stability constant ($\overline{K}_{ML}$) and M/ML diffusion transport coefficients (D_M, D_{ML} or ε), the M and ML concentration profiles $c_{i=M,ML}(r)$ were obtained by solving numerically Eqs. (8)-(12) via the collocation

procedure implemented in COLSYS package [48,49,54]. The lability index ξ was then evaluated from Eq. (14) and a FORTAN program written for that purpose is available upon request. Correctness of the obtained numerical results was systematically addressed from their comparison to the explicit analytical solutions we derived for Eq. (8) in some limiting kinetic and electrostatic scenarios we detail below.

2.2. Analytical expressions of ML lability index for limiting kinetic and electrostatic cases.

2.2.1. Case where ML is inert.

This situation is reached when criteria defined by Eq. (2) are satisfied. ML complexes then do not contribute in any way to the transfer of M from the bulk medium to the reactive interface, even in the presence of a large excess of ML in the medium. Eq. (7b) becomes immaterial and the situation is identical to the one where the free metal ion concentration is the total metal concentration, i.e. the 'free metal only' scenario. The dimensionless M concentration profile $\overline{c}_{\mathrm{M}}(r)=c_{\mathrm{M}}(r)/c_{\mathrm{M}}^{*}$ under M-sink condition then reads as [48,49]

$$\overline{c}_{\mathrm{M}}(r)=\beta_{\mathrm{M}}(r)\left[1-F_{r,r_{\mathrm{c}}}/F_{a,r_{\mathrm{c}}}\right] \tag{15}$$

where the radial function *F* is defined by the integral equation $F_{r_1,r_2}=\int_{r_1}^{r_2}\zeta^{-2}\beta_{\mathrm{M}}^{-1}(\zeta)\mathrm{d}\zeta$ (m^{-1}) with $\beta_{\mathrm{M}}(r)=\mathrm{e}^{-z_{\mathrm{M}}y(r)/z}$ the Boltzmann factor pertaining to M at position *r* and ζ is a dummy integration variable. Eq. (15) is the solution of Eq. (7a) devoid of the associative and dissociative kinetic terms, with the solution being valid for any form of $y(r)$. Using Eq. (9) in the absence of ML, we obtain for the M accumulation flux at the particle surface

$$J_{\mathrm{M}}(r=a)=f_{\mathrm{el,M}}D_{\mathrm{M}}c_{\mathrm{M}}^{*}/a \tag{16}$$

where $f_{\mathrm{el,M}}=1/\left(aF_{a,r_{\mathrm{c}}}\right)$ is a dimensionless scalar that quantifies the impact of the interfacial electrostatic field on M diffusion process [55], with $f_{\mathrm{el,M}}$ values greater (lower) than unity representing a conductive accelerating (retarding, respectively) effect depending on the sign of the product $z_{\mathrm{M}}\times y_{\mathrm{a}}$. For a potential distribution $y(r)$ given by the Debye-Hückel formulation of the PB equation (Eq. (13)), $f_{\mathrm{el,M}}$ simplifies into

$$f_{\mathrm{el,M}}\approx 1-z^{-1}z_{\mathrm{M}}y_{\mathrm{a}}/(\kappa a) \tag{17}$$

Accordingly, the effect of the electric double layer field on the dynamics of M diffusion to a charged reactive microparticle (with $\kappa a>>1$) remains basically insignificant ($f_{\mathrm{el,M}}\approx 1$) simply because the corresponding diffusion layer of thickness *a* then extends well above the Debye layer region.

2.2.2. Case where particle electrostatics is completely screened.

Under complete electrostatic screening conditions, the potential distribution verifies $y(r)\to 0$, which applies to either uncharged particles ($y_{\mathrm{a}}\to 0$) or particles whose surface charge is significantly screened by

background electrolyte ions ($1/\kappa \to 0$). Following the methodology in [53], solving Eqs. (8)-(11) in the limit $y(r) \to 0$ leads to the following exact expressions for the M and ML concentration profiles $\bar{c}_{i=M,ML}(r) = c_i(r)/c_i^*$

$$\bar{c}_M(r) = 1 - \frac{a}{r}\frac{\varepsilon\bar{K}_{ML}\left[e^{\bar{h}_a(1-r/a)} - (1-\alpha)e^{-\bar{h}_a(1-r/a)}\right] + \left[\alpha + \bar{h}_a(2-\alpha)\right](1-\phi^{1/3}r/a)}{\alpha\varepsilon\bar{K}_{ML} + \left[\alpha + \bar{h}_a(2-\alpha)\right](1-\phi^{1/3})} \quad (18)$$

$$\bar{c}_{ML}(r) = 1 - \frac{a}{r}\frac{\left[\alpha + \bar{h}_a(2-\alpha)\right](1-\phi^{1/3}r/a) - \left[e^{\bar{h}_a(1-r/a)} - (1-\alpha)e^{-\bar{h}_a(1-r/a)}\right]}{\alpha\varepsilon\bar{K}_{ML} + \left[\alpha + \bar{h}_a(2-\alpha)\right](1-\phi^{1/3})} \quad (19)$$

where $\alpha = 1 - e^{2\bar{h}_a(1-\phi^{-1/3})}$ and $\bar{h}_a$ (dimensionless) is related to the Damköhler number $\bar{\kappa}_a = D_M^{-1}k_a c_L^* a^2$ by

$$\bar{h}_a = \sqrt{\bar{\kappa}_a}\sqrt{1 + 1/(\varepsilon\bar{K}_{ML})} \quad (20)$$

Application of Eq. (9) then provides the M transport flux at $r = a$ for $y(r) \to 0$

$$J_M(r=a) = D_M c_M^* p/a \quad (21)$$

where p (dimensionless) quantifies the contribution of ML dissociation at the particle surface to the flux according to $p = 1 + \varepsilon\bar{K}_{ML}\xi$, with the lability parameter ξ defined by combining Eq. (14) in the limit $\beta_{ML}^a = \beta_{ML}(r=a) \to 1$ with Eq. (19) taken at $r = a$, i.e.

$$\xi = \frac{(1-\phi^{1/3})\left(1 + \bar{h}_a \coth\left[\bar{h}_a(\phi^{-1/3}-1)\right]\right) - 1}{\varepsilon\bar{K}_{ML} + (1-\phi^{1/3})\left(1 + \bar{h}_a \coth\left[\bar{h}_a(\phi^{-1/3}-1)\right]\right)} \quad (22)$$

For dilute suspensions of reactive particles ($\phi << 1$), Eq. (22) reduces to

$$\xi = \sqrt{\bar{\kappa}_a}/\left(\sqrt{\bar{\kappa}_a} + \sqrt{\varepsilon\bar{K}_{ML}}\sqrt{1+\varepsilon\bar{K}_{ML}}\right) \quad (23)$$

which consistently reproduces the result given by Galceran et al. [53] for the semiininfinite diffusion case. Eq. (23) allows a refinement of the dynamic criteria established by Eqs. (1)-(6) to discriminate inert from dynamic ML complexes, and differentiate for the latter the kinetics-diffusion conditions in line with a labile or non-labile ML system [50]. Namely, for $\bar{\kappa}_a \to 0$ (i.e. $\xi = 0$ and $p = 1$), the flux $J_M(r=a)$ (Eq. (21)) reduces to $J_M(r=a) = D_M c_M^*/a$: this is essentially the 'free metal only case' examined in §2.2.1 with account for electrostatics and where ML behaves as if it is inert. The other extreme $\bar{\kappa}_a >> 1$ refers to dynamic ML complexes, and two limiting behaviors can be distinguished depending on the nature of the ML contributing flux. In detail, for $\bar{\kappa}_a >> (\varepsilon\bar{K}_{ML})(1+\varepsilon\bar{K}_{ML})$, we have $\xi \to 1$ and the M surface flux reduces to J_{dif} defined by Eq. (4) (with $a << \bar{\delta}$): this is the fully labile ML case. For $\bar{\kappa}_a << (\varepsilon\bar{K}_{ML})(1+\varepsilon\bar{K}_{ML})$, which implies $\varepsilon\bar{K}_{ML} >> 1$ to satisfy the examined limit $\bar{\kappa}_a >> 1$, ξ and $J_M(r=a)$ reduces to $\xi \to \bar{\kappa}_a^{1/2}/(\varepsilon\bar{K}_{ML})$ and $J_M(r=a) \to D_M c_M^*/a + J_{kin}$ with J_{kin} given by Eq. (6): this is the nonlabile ML scenario where M accumulation is dictated by both diffusion of free M *and* kinetics of ML dissociation.

2.2.3. Case $\kappa\mu_o >> 1$ within the Debye-Hückel electrostatic limit.

In the absence of specific interactions between ions from the background electrolyte and ligand L, the intuitive relationship $z_{ML} = z_M + z_L$ between charges carried by ML and L is expected. However, when such

interactions are operative (cf. e.g. [30]), ion-pairing will alter the pristine charge carried by L and it is the resulting effective (or net) charge that drives the conduction-diffusion of ion-paired ligands through the electric double layer at the particle/medium interface. Accordingly, depending on the electrolyte composition and chemical nature of L, situations may arise where both L and ML are effectively uncharged (i.e. $\beta_{\mathrm{L}}(r)\to 1$ and $z_{\mathrm{ML}}=0$ in Eq. (8b)) whereas $z_{\mathrm{M}}>0$. The developments in this section apply to such a situation where Eq. (8) then reduces to

$$\begin{cases}\nabla_r^2\left[\overline{c}_{\mathrm{M}}(r)+\varepsilon\overline{K}_{\mathrm{ML}}\overline{c}_{\mathrm{ML}}(r)\right]+z^{-1}z_{\mathrm{M}}\left\{\overline{c}_{\mathrm{M}}(r)\nabla_r^2 y(r)+\left[\left(\mathrm{d}y(r)/\mathrm{d}r\right)\left(\mathrm{d}\overline{c}_{\mathrm{M}}(r)/\mathrm{d}r\right)\right]\right\}=0 & \text{(a)}\\ \mathrm{d}^2\omega_{\mathrm{ML}}(r)/\mathrm{d}r^2-\gamma\left[\omega_{\mathrm{ML}}(r)-\omega_{\mathrm{M}}(r)\right]=0 & \text{(b)}\end{cases} \tag{24}$$

where we introduced $\gamma=\overline{\kappa}_{\mathrm{a}}/\left(a^2\varepsilon\overline{K}_{\mathrm{ML}}\right)$ (m^{-2}). After some algebra, the solution $c_{\mathrm{M}}(r)$ of Eq. (24a) can be written in the general form

$$\overline{c}_{\mathrm{M}}(r)/\beta_{\mathrm{M}}(r)=\left(c_1+c_2F_{a,r}\right)-\varepsilon\overline{K}_{\mathrm{ML}}\left(\overline{c}_{\mathrm{ML}}(r)+\int_a^r\left(\left[\beta_{\mathrm{M}}(\zeta)\right]^{-1}-1\right)\left(\mathrm{d}\overline{c}_{\mathrm{ML}}(\zeta)/\mathrm{d}\zeta\right)\mathrm{d}\zeta\right) \tag{25}$$

where c_1 (dimensionless) and c_2 (m) are constants, and the integral function $F_{a,r}$ was defined in §2.2.1. Outside the electric double layer, i.e. for $\kappa(r-a)>>1$, we have $y(r)\to 0$ and $\beta_{\mathrm{M}}(r)\to 1$ so that the integral in Eq. (25) becomes 0. This integral term can therefore deviate from a value of 0 only within the double layer domain, and the magnitude of this deviation depends on the applicable ML concentration gradient therein. Within the conventional Koutecký-Koryta approximation *without electrostatics included*, ML depletion in the reaction layer of thickness μ_{o} is insignificant. Accordingly, under the condition $\kappa\mu_{\mathrm{o}}>>1$ which reflects weak overlap between the reaction layer and the electric double layer, the integral in Eq. (25) can be safely neglected, and we then infer

$$\omega_{\mathrm{M}}(r)=r\beta_{\mathrm{M}}(r)\left(c_1+c_2F_{a,r}\right)-\varepsilon\overline{K}_{\mathrm{ML}}\beta_{\mathrm{M}}(r)\omega_{\mathrm{ML}}(r) \tag{26}$$

Substituting Eq. (26) into Eq. (24b), and retaining the Debye-Hückel form of $\beta_{\mathrm{M}}(r)$, i.e. $\beta_{\mathrm{M}}(r)\sim 1-z_{\mathrm{M}}y(r)/z$ with $y(r)$ given by Eq. (13), we then show after some lengthy algebra that $\omega_{\mathrm{ML}}(r)=r\overline{c}_{\mathrm{ML}}(r)$ is defined by a non-homogeneous Bessel differential equation whose solution is

$$\overline{c}_{\mathrm{ML}}\left(\overline{X}_r\right)=\alpha_1 r^{-1}J_\lambda\left(-i^{\mathrm{k}}X_r\right)+\alpha_2 r^{-1}Y_\lambda\left(-i^{\mathrm{k}}\overline{X}_r\right)+\pi r^{-1}\frac{\gamma}{\kappa}\left\{Y_\lambda\left(-i^{\mathrm{k}}\overline{X}_r\right)\int_a^r\Lambda(\varsigma)J_\lambda\left(-i^{\mathrm{k}}\overline{X}_\varsigma\right)\mathrm{d}\varsigma-J_\lambda\left(-i^{\mathrm{k}}\overline{X}_r\right)\int_a^r\Lambda(\varsigma)Y_\lambda\left(-i^{\mathrm{k}}\overline{X}_\varsigma\right)\mathrm{d}\varsigma\right\} \tag{27}$$

, where $\alpha_{1,2}$ (m) are constants, (cursive) *i* denotes the imaginary number ($i^2=-1$), index k verifies k=2 for $y_{\mathrm{a}}>0$ and k=1 for $y_{\mathrm{a}}<0$, and the radial function $\Lambda(r)$ (m) in Eq. (27) is further defined by $\Lambda(r)=r\beta_{\mathrm{M}}(r)\left(c_1+c_2F_{a,r}\right)$. J_λ and Y_λ are the unmodified Bessel functions of the first and second type with order λ (dimensionless) that compares the respective thickness of the reaction layer and Debye layer according to

$$\lambda=2\left(\kappa\mu_{\mathrm{o}}\right)^{-1}\sqrt{1+\left(\varepsilon\overline{K}_{\mathrm{ML}}\right)^{-1}} \tag{28}$$

The space variable $\overline{X}_r$ (dimensionless) in Eq. (27) also involves the $\kappa\mu_{\mathrm{o}}$ term and depends on *r* via

$$\overline{X}_r=2\left(\kappa\mu_{\mathrm{o}}\right)^{-1}\sqrt{z^{-1}z_{\mathrm{M}}\left|y_{\mathrm{a}}\right|}\mathrm{e}^{-\kappa(r-a)/2} \tag{29}$$

The set of constants $c_{1,2}$ and $\alpha_{1,2}$ are determined from proper application of the boundaries defined by Eqs. (10) and (11) for the here-examined $z_{ML}=0$ case (cf. details in **Supplementary Material, SM**). Obviously, the M concentration profile $\bar{c}_M(r)=\omega_M(r)/r$ directly follows from combination of Eqs. (26)-(27). The Bessel differential equation with solution provided by Eq. (27) displays an irregular singularity for $\bar{X}_r \to \infty$, which is achieved for $\kappa\mu_o << 1$, and a regular singularity for $\bar{X}_r = 0$, or equivalently $y_a = 0$. The former singularity corresponds to a reaction layer that recedes deep inside the electrical Debye layer, and this scenario is not covered by Eq. (26) as then the integral term in Eq. (25) would deviate significantly from 0. The latter singularity actually corresponds to the situation treated in §2.2.2. Using the Taylor developments $J_\lambda\left(-i^k X_r\right) \to \left[2^\lambda \Gamma(1+\lambda)\right]^{-1}\left(-i^k \bar{X}_r\right)^\lambda$ and $Y_\lambda\left(-i^k \bar{X}_r\right) \to -2^\lambda \pi^{-1}\Gamma(\lambda)\left(-i^k \bar{X}_r\right)^{-\lambda}$ valid for $\bar{X}_r \to 0$ where Γ is the Gamma function, we verified indeed that Eqs. (26)-(27) considered in the limit $y_a \to 0$ reduce to the M and ML concentration profiles given by Eqs. (18)-(19). Finally, applying Eq. (14) with use of Eq. (27), we obtain for the lability index ξ

$$\xi = \mathrm{Re}\left(1 - a^{-1}\left\{\alpha_1 J_\lambda\left(-i^k 2(\kappa\mu_o)^{-1}\sqrt{z^{-1}z_M|y_a|}\right) + \alpha_2 Y_\lambda\left(-i^k 2(\kappa\mu_o)^{-1}\sqrt{z^{-1}z_M|y_a|}\right)\right\}\right) \quad (30)$$

where $\beta_M^a = \beta_M(r=a)$, the defining expressions of $\alpha_{1,2}$ together with those for $c_{1,2}$ are given in **SM**, and the notation 'Re(…)' means 'real part of (…)'. Using Eq. (9), it can be shown that the M flux at the surface of the reactive microparticle is given by $J_M(r=a) = D_M c_M^* c_2 / a^2$, which leads for positively charged particles to

$$J_M(r=a) = \frac{\left(1+\varepsilon\bar{K}_{ML}\right) f_{el,M} D_M c_M^*}{a}\mathrm{Re}\left(\frac{1 + U_{a,c}\varepsilon\bar{K}_{ML}\sqrt{z^{-1}z_M\bar{\kappa}_a|y_a|}\,a^{-1}\left(I_1^c - \dfrac{r_c}{1+\varepsilon\bar{K}_{ML}}\right)}{1 + U_{a,c}\varepsilon\bar{K}_{ML}\sqrt{z^{-1}z_M\bar{\kappa}_a|y_a|}\,a^{-1}\left(I_1^c - F_{a,r_c}^{-1} I_2^c\right)}\right) \quad (31)$$

where the terms $U_{a,c}$ (dimensionless), I_1^c (m) and I_2^c (dimensionless) depend on the particle electrostatic descriptors $1/\kappa$ and y_a, and on the dimensionless kinetic constant $\bar{\kappa}_a$ according to Eqs. (S8)-(S9) and Eqs. (S16)-(S20) in **SM**, respectively. The procedure to adapt Eq. (31) to the case $y_a < 0$ is detailed in the **SM**. In the limit where ML is inert (i.e. the case retrieved for $\bar{K}_{ML} \to 0$), Eq. (31) correctly reduces to Eq. (16).

3. Results and discussion.

In the following sections, the dependence of the lability index ξ on particle electrostatics, M-ML chemical kinetics and transport, is detailed for uncharged (§3.1) and charged (§3.2) complexes ML and ligands L. For the latter case, we differentiate situations where the charge neutralization of L by M ($z_M > 0$) is insignificant (i.e. $z_{ML} = z_L$, §3.2.1) or not ($z_{ML} = z_L + z_M$, §3.2.2). In line with arguments in §2.2.3, we recall that the achievement of these different ML/L charge configurations is connected to the nature of L and to the extent of pairing of L and/or ML with ions from the background electrolyte.

3.1. Uncharged metal complexes and ligands ($z_{ML} = z_L = 0$).

For given values of the Debye layer thickness $1/\kappa$ and particle radius *a* (with $\kappa a >> 1$), **Figure 2** reports variations of ξ (Eqs. (8), (10)-(12), (14)) over a large range of $\bar{\kappa}_a = D_M^{-1} k_a c_L^* a^2$, thereby covering all possible scenarios depending on the nature of M (and associated k_a value) and on the respective extensions of the reaction and diffusion layers with thicknesses μ_o (Eq. (5)) and *a*, respectively. Results are plotted in semi-log representation as a function of $\kappa\mu_o$ which reflects the magnitude of the overlap between these two interfacial layers. **Figure 2A** evidences a sigmoidal decrease of ξ from $\xi \to 1$ to $\xi \to 0$ at fixed particle surface potential y_a with increasing $\kappa\mu_o$ from $\kappa\mu_o \to 0$ to $\kappa\mu_o \to \infty$. These asymptotic limits correspond to the fully labile and nonlabile ML cases, respectively, and they are achieved irrespectively of y_a. The uncharged particle case (dotted line) is correctly reproduced by the analytical expression of ξ defined by Eq. (23). At fixed $\kappa\mu_o$, ML lability index increases upon making the surface potential y_a more negative, i.e. more attractive for the metal ion. Conversely, taking the case of an uncharged particle as a reference, ML loses lability with a particle surface that becomes more positively charged. The amplitude of the observed modulations in ξ at fixed $\kappa\mu_o$ is more significant for $y_a > 0$, which makes the dependence of ξ on y_a asymmetric, especially at values of $\kappa\mu_o$ close to unity. Accordingly, the nonlabile ML limit $\xi \to 0$ is reached at lower values of $\kappa\mu_o$ for sufficiently large $y_a (>0)$ as compared to the case $y_a \le 0$. **Figure 2A** thus shows that repulsive (attractive) interactions between M and reactive particle lead to a decrease (increase, respectively) of ML lability or, equivalently, to an increased contribution of ML dissociation kinetics (diffusion, respectively) to the M accumulation flux at the particle surface. **Figures 2B-2C** highlight how the sigmoidal dependence of ξ on $\kappa\mu_o$ for y_a = -2, 0 and 2 is impacted by $\bar{K}_{ML}$ and $\varepsilon = D_{ML}/D_M$. An increase in $\bar{K}_{ML}$ or ε for any of the tested y_a implies a decrease in ξ at fixed $\kappa\mu_o$, which is in agreement with inspection of Eq. (23) valid for $y_a = 0$. Qualitatively, this finding is explained by a corresponding significant decrease of the ratio J_{kin}/J_{dif} (Eq. (3)) as a result of either decreasing J_{kin} (Eq. (6)) due to decrease in k_d (**Figure 2B**), or increasing J_{dif} (Eq. (4)) due to increase of D_{ML} (**Figure 2C**). In turn, M transfer from bulk solution to the particle becomes increasingly limited by ML dissociation kinetics. For the sake of completeness, **Figures 2B-2C** display the expected variation of ξ on $\kappa\mu_o$ for uncharged particles and fully nonlabile ML complex, i.e. $\xi \to \bar{\kappa}_a^{1/2} / (\varepsilon \bar{K}_{ML})$ (cf. §2.2.2) : numerically evaluated ξ consistently converges to this analytical limit at sufficiently large $\kappa\mu_o$ where nonlability of ML is significant.

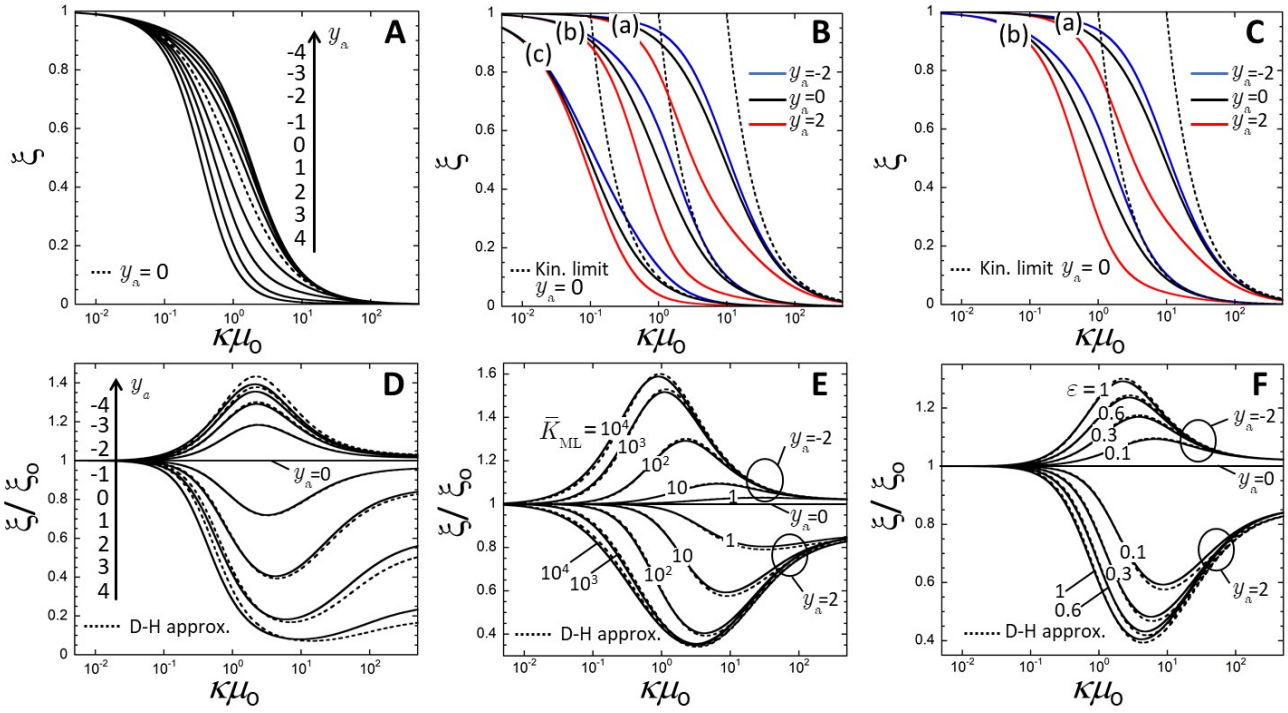

Figure 2. Dependence of ML lability index ξ on y_a (indicated) (**A**), and on $\bar{K}_{ML}$ (**B**) and $\varepsilon = D_{ML}/D_M$ (**C**) for y_a = -2, 0 and 2 (indicated), as a function of $\kappa\mu_o$. In (**B**): $\bar{K}_{ML}$ = 10 (a), 10^2 (b), 10^3 (c). In (**C**): ε = 0.1 (a), 1 (b). Dotted lines in (**A**) and (**B**)-(**C**) refer to the uncharged particle case (Eq. (23)) and to the kinetic limit $\xi \to \bar{\kappa}_a^{1/2}/\left(\varepsilon\bar{K}_{ML}\right)$, respectively. Panels (**D**), (**E**) and (**F**) report (and extend) results of (**A**), (**B**) and (**C**) in the form ξ/ξ_o where ξ_o is the ML lability index at $y_a = 0$. Dotted lines in (**D**)-(**F**) are predictions using the linearized Debye-Hückel (denoted as 'D-H') expression of $y(r)$ (Eq. (13)). (**A**)-(**F**): solid lines refer to results from numerical solving of Eqs. (8), (10)-(12)/(13), (14). Unless otherwise specified, adopted model parameters are: $1/\kappa$ = 10 nm, a = 1 μm, r_c/a = 50, ε = 1, $\bar{K}_{ML}$ = 10^2, $z_M = 2$, $z_{ML} = z_L = 0$.

To quantify the relative changes in ξ mediated by particle electrostatics *as compared to* the situation where the particle is uncharged, **Figures 2D**, **2E** and **2F** display and extend the results of **Figures 2A, 2B** and **2C**, respectively, in the form ξ/ξ_o where ξ_o is the ML lability index for $y_a \to 0$. **Figure 2D** confirms the asymmetry in the dependence of ξ on y_a at given $\kappa\mu_o$, and it further illustrates the correctness of the Debye-Hückel form of $y(r)$ (Eq. (13)) in reproducing the results obtained with the non-linearized expression of $y(r)$ (Eq. (12)), even for $|y_a| > 1$ (this conclusion also holds for **Figures 2E-2F**). This finding may seem counterintuitive given the range of $|y_a|$ that legitimates the use of Eq. (13). It is explained by the decreasing contribution of the particle electrostatic field to the interfacial M (and therewith ML) concentration profiles upon increasing $\kappa\mu_o$, i.e. extending the reaction layer further away from the Debye layer. In addition, at sufficiently low (high) $\kappa\mu_o$, ξ/ξ_o becomes necessarily independent of y_a as then ML complex becomes fully labile (nonlabile) with the associated limits $\xi/\xi_o \to 1$ ($\xi/\xi_o \to 0$, respectively). **Figures 2E-2F** further evidence that for a given setting of M-particle attraction (repulsion) and $\kappa\mu_o$, there is a relative gain (loss, respectively) in ML lability with increasing $\bar{K}_{ML}$ or ε *as compared to* the corresponding case where the particle is uncharged. As confirmed by the analysis of the corresponding M/ML concentration profiles (**Figure**

S1 in **SM**), these relative variations of the lability captured by the ratio ξ / ξ_o originate from the higher (lower) ML concentration in the close vicinity of the particle surface (*as compared to* the uncharged particle case) upon promoting M-particle repulsion (attraction, respectively). This electrostatics-induced buffering (depletion, respectively) of ML at the particle/medium interface (and the associated decrease (increase) in lability) is enhanced for increasing values of $\bar{K}_{ML}$ or ε *in comparison to* the corresponding situations where $y_a = 0$ (**Figure S1)**.

Figure 3A details how the double layer thickness $1/\kappa$ impacts on ξ for y_a = -2, 0 and 2, all other relevant parameters of the system being fixed. At fixed y_a and given $\kappa\mu_o$, the lability index ξ decreases with increasing $1/\kappa$. Qualitatively, this dependence is explained by the $\kappa\mu_o$ scaling adopted in abscissa, which generates a shift of the curves ξ versus $\kappa\mu_o$ to the left with increasing κ^{-1} at given μ_o. Unlike the trivial case $y_a = 0$, the dependence of ML lability index on $\kappa\mu_o$ for $y_a \neq 0$ does not simply reduce to the above scaling, which is highlighted in **Figure 3B** where the data of **Figure 3A** are reported after normalization of ξ by ξ_o. As expected, ξ / ξ_o is independent of κ^{-1} for $y_a = 0$ (with resulting $\xi / \xi_o = 1$) while increasing values of κ^{-1} generate a relative gain (loss) in ML lability for scenario where M-particle attraction (repulsion, respectively) prevails. Said otherwise, as the ionic strength of the medium decreases, the surface charge experienced by M is effectively greater due to the decreased electrostatic screening by the background electrolyte. The maximal gain/loss in lability is shifted to lower $\kappa\mu_o$ with increasing κ^{-1} as a result of the scaling invoked above. In other words, the effect associated with an increase of κ^{-1} at given $|y_a| \neq 0$ is qualitatively similar to that caused by increasing $|y_a|$ at given κ^{-1} (**Figure 2D**). This correspondence highlights the dynamic nature of the lability parameter and the way in which the interfacial electric field $dy(r)/dr|_{r=a}$ affects M/ML concentration polarization (see Eq. (7)). For illustration, we have indeed $dy(r)/dr|_{r=a} \sim -\kappa y_a$ in the Debye-Hückel approximation so that ξ / ξ_o is expected to actually depend on κy_a, in accordance with numerical results. In contrast, equilibrium BLM and FIAM frameworks, when properly corrected for particle electrostatics, solely involve the Boltzmann enhancement (and thereby y_a) of the M/ML concentration at the particle surface, thus ignoring the impacts of the interfacial electric field on M and ML surface concentrations. Finally, we report in **Figure 3C** the variations of ξ / ξ_o versus y_a at $\kappa\mu_o = 1$, 10 and 10^2 with or without assuming Debye-Hückel expression for $y(r)$ (Eq. (13)) and with including comparison to predictions from Eq. (30). Beyond the features already discussed in the preceding figures (i.e. an asymmetric dependence of ξ / ξ_o on y_a that is more or less pronounced depending on $\kappa\mu_o$ and the correctness in applying Eq. (13) to approximate the results derived with Eq.(12), **Figure 3C** shows that Eq. (30) properly reproduces ξ / ξ_o at sufficiently small $|y_a|$ *and* large $\kappa\mu_o$, which is fully consistent with the conditions validating the application of Eq. (30). In detail, Eq. (30) actually corresponds to the equation of the tangent to the curve ξ / ξ_o vs. y_a at

$y_a \to 0$. Similar conclusions are obtained in **Figure 3D** where ξ / ξ_o is plotted as a function of y_a for $\kappa\mu_o = 10$ and different values of κ^{-1}.

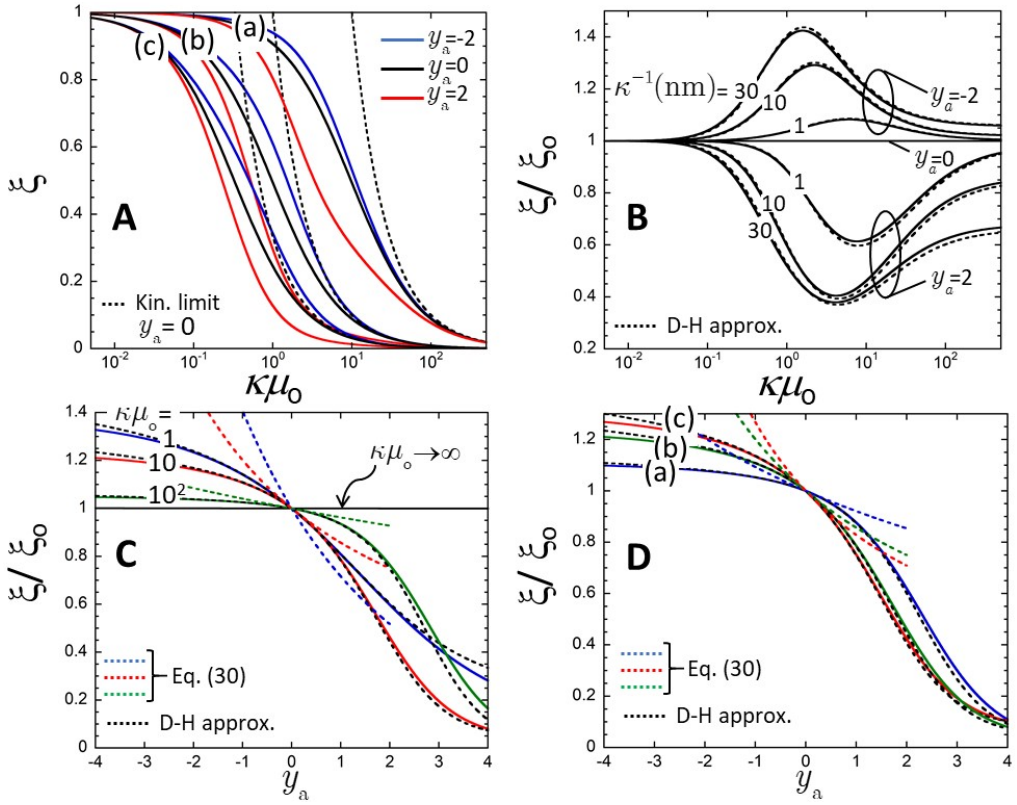

Figure 3. (A) Dependence of ξ on y_a (indicated) and κ^{-1} as a function of $\kappa\mu_o$. $1/\kappa = 1$ nm (a), 10 nm (b), 30 nm (c). (**B**) As in (**A**) for ξ / ξ_o. Dotted lines in (**A**) and (**B**) refer to the kinetic limit $\xi \to \bar{\kappa}_a^{1/2} / \left(\varepsilon \bar{K}_{ML}\right)$ and to predictions with linearized Debye-Hückel (D-H) expression of $y(r)$ (Eq. (13)), respectively. (**C**) ξ / ξ_o versus y_a for different $\kappa\mu_o$ (indicated) and $1/\kappa = 10$ nm. (**D**) ξ / ξ_o versus y_a for $1/\kappa = 1$ nm (a), 10 nm (b), 30 nm (c) and $\kappa\mu_o = 10$. Black and colored dotted lines in (**C**) and (**D**) refer to predictions within D-H framework and with using Eq. (30), respectively. (**A**)-(**D**): colored solid lines are results from numerical solving of Eqs. (8), (10)-(12)/(13), (14). Unless otherwise specified, model parameters are: $1/\kappa = 10$ nm, $a = 1$ μm, $r_c / a = 50$, $\varepsilon = 1$, $\bar{K}_{ML} = 10^2$, $z_M = 2$, $z_{ML} = z_L = 0$.

Finally, we emphasize in **Figure 4** the connections between lability index ξ (Eq. (14)) and associated M/ML concentrations profiles under selected $\kappa\mu_o$ and y_a conditions. Results for $\bar{c}_{i=M,ML}(r) = c_i(r) / c_i^*$ are reported as a function of the scaled space variable $(r-a)/\mu_o$ (**Figures 4A-4C**) and $(r-a)/a$ (**Figures S2A-S2C** in **SM**). Starting with the case $y_a = 0$ (**Figure 4B**), increasing $\kappa\mu_o$ at fixed κ^{-1} comes to increase the thickness of the reaction layer, that is extending the interfacial region where the equilibrium relationship $c_{ML}(r) / c_M(r) = K_{ML} c_L^*$ (or, equivalently, $\bar{c}_{ML}(r) / \bar{c}_M(r) = 1$) does *not* apply (**Figure S2B**). As a result, ML depletion at the particle surface is reduced with increasing $\kappa\mu_o$, and ML lability index ξ decreases (**Figure 4B**), in line with the conclusions from **Figure 2**. In the fully labile limit $\xi \to 1$ reached for $\kappa\mu_o << 1$, equilibrium between M and ML is maintained all along their diffusion to the particle surface. The equality $\bar{c}_{ML}(r) / \bar{c}_M(r) = 1$ then holds everywhere at the particle/medium interface and, in turn, sink conditions at the particle surface hold for both M *and* ML species ($\bar{c}_{i=M,ML}(r=a) = 0$). These features are qualitatively maintained when particle

electrostatics comes into the picture (**Figures 4A,4C**). On a quantitative level, attractive M-particle interactions (**Figure 4A**) increases M surface flux and accumulation at $r = a$ (Eq. (9), cf. §3.2.2), thereby forcing ML to dissociate to satisfy the electrostatics-induced demand in M. As a result, ML depletion at the particle surface is enhanced, and ξ increases as compared to the case of an uncharged particle. Obviously, this effect is most pronounced at intermediate $\kappa\mu_o$ where ML is neither fully labile nor fully nonlabile. Conversely, any electrostatic repulsion between M and particle surface, combined with the sink condition imposed for the M species at $r = a$ (**Figure 4C**), results in a maximum reached by $\bar{c}_M(r)$ for intermediate $\kappa\mu_o$ where there is significant overlap between reaction and electric double layers. In turn, the electric double layer field contributes to reduce ML depletion at the particle/medium interface in comparison to the situation $y_a = 0$, and ML lability is therefore diminished. These properties are further illustrated by **Figure S3** in **SM** where $\bar{c}_{i=M,ML}(r)$ profiles are plotted for $\kappa\mu_o = 10^{-2}$, 1 and 10 and a detailed sequence of y_a values.

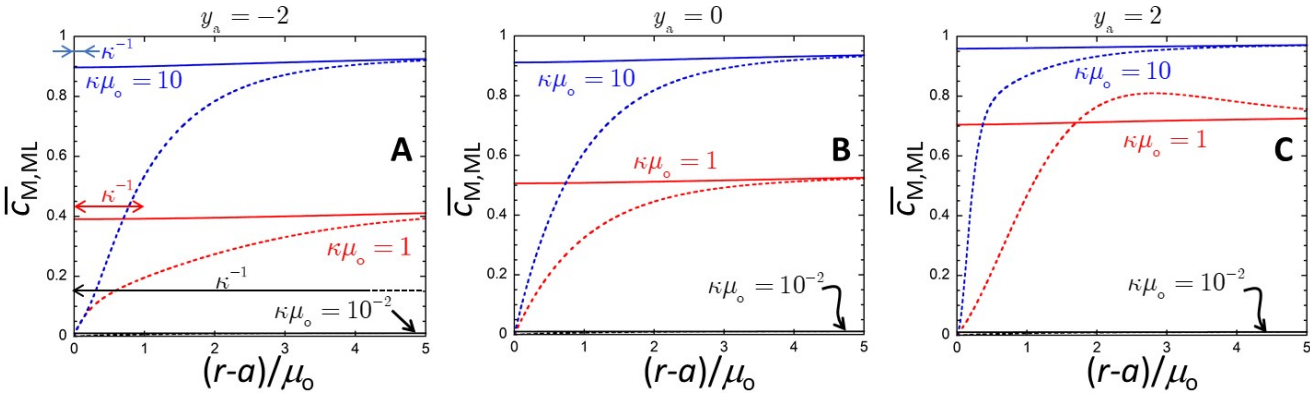

Figure 4. Spatial distributions of the concentration profiles $\bar{c}_M(r) = c_M(r)/c_M^*$ (dotted lines) and $\bar{c}_{ML}(r) = c_{ML}(r)/c_{ML}^*$ (solid lines) for y_a = -2 (**A**), 0 (**B**) and 2 (**C**) plotted as a function of the scaled space variable $(r-a)/\mu_o$ for $\kappa\mu_o = 10$ (blue), 1 (red) and 10^{-2} (black). Dotted and solid black curves for $\bar{c}_M(r)$ and $\bar{c}_{ML}(r)$, respectively, are confounded for $\kappa\mu_o = 10^{-2}$ (this is the fully labile limit, $\xi \to 1$). Adopted model parameters are $1/\kappa = 10$ nm, $a = 1$ µm, $r_c/a = 50$, $\varepsilon = 1$, $\bar{K}_{ML} = 10^2$, $z_M = 2$, $z_{ML} = z_L = 0$. The Debye layer region of thickness κ^{-1} is indicated in panel (**A**) for the three $\kappa\mu_o$-conditions examined.

3.2. Charged metal ligands.

3.2.1. Case of insignificant neutralization of ligand charge by metal ion ($z_{ML} = z_L$).

We analyse here how electrostatic interactions between particle surface, ML, M and L species affect ML lability index ξ. **Figure 5A** reports ξ as a function of $\kappa\mu_o$ for values of $z_{ML}(=z_L)$ differing with respect to both magnitude and sign (while maintaining $z_M = 2$). The case of negatively charged particle (y_a = -2) is considered, and corresponding M and ML concentration profiles are given in **Figures 5B-5C** at $\kappa\mu_o = 1$ for illustration. **Figure 5A** evidences that attractive interactions between ML and the particle (i.e. for $z_{ML}(=z_L) > 0$) increase ML lability at fixed $\kappa\mu_o$, and this gain in lability thus adds to that generated by M-particle attraction (cf. **Figure 2A**). In turn, the fully labile limit $\xi \to 1$ is reached over an increasing range of $\kappa\mu_o$ values with increasingly positive z_{ML}. As a result, the curves ξ vs. $\kappa\mu_o$ become increasingly shifted to the right as $z_{ML}(>0)$

becomes more positive. Comparison with the results obtained for $z_{ML}=0$ supports the finding that ML lability is significantly enhanced when ML carries a positive charge. As detailed below for the case $z_{ML}(=z_L)<0$, this significant gain in ML lability at given $\kappa\mu_o$ is also favored by an increase in the equilibrium concentration of L $(z_L>0)$ at the particle surface. For the reasons detailed in §3.1, ξ decreases with $\kappa\mu_o$ at given $z_{ML}>0$ following a sigmoid-like dependence. With increasingly positive z_{ML}, the accumulation of charged ML species at the particle surface becomes significant. It remains however less than that dictated by the equilibrium Boltzmann factor $\beta_{ML}(r=a)>>1$ because of ML dissociation-supported consumption of M at the particle surface. The increase in $\bar{c}_{ML}$ at $r=a$ due to attractive electrostatics is clearly observed in the ML concentration profiles (**Figure 5B**), and it is associated with a local maximum reached by $\bar{c}_M$ in the direct vicinity of the particle surface (**Figure 5C**). For sufficiently labile ML, $\bar{c}_{ML}(r=a)$ does not follow the z_{ML}-sequence expected from simple thermodynamic considerations (i.e. from the expected variation of $\beta_{ML}(r=a)$ with changing z_{ML}) due to fast ML dissociation kinetics.

The scenario where repulsive interactions between ML/L and the particle (i.e. $z_{ML}(=z_L)<0$) take place is marked by a lower ML lability index ξ at given $\kappa\mu_o$ as compared to the corresponding $z_{ML}>0$ case (**Figure 5A**). At sufficiently large $\kappa\mu_o$ where the Debye layer is immaterial at the scale of the reaction layer, ML is significantly nonlabile, ξ becomes independent of particle electrostatics and of $z_{ML}(=z_L)$: ξ then approaches the kinetic regime defined by $\xi\to\bar{\kappa}_a^{1/2}/(\varepsilon\bar{K}_{ML})$ (§2.2.2). More interestingly, we observe at sufficiently small $\kappa\mu_o$ and for $z_{ML}(=z_L)<0$ a non-monotonous dependence of ξ on $\kappa\mu_o$ (**Figure 5A**). Namely, taking the example $z_{ML}(=z_L)$=-2, ξ first decreases with increasing $\kappa\mu_o$, in line with an extension of the nonlabile region from the particle surface, then ξ increases at larger $\kappa\mu_o$ to reach a local maximum, before approaching the kinetic limit invoked above for $\kappa\mu_o>>1$. For $z_{ML}(=z_L)$=-3, the initial decrease in ξ with increasing $\kappa\mu_o$ even vanishes and a well-defined maximum is only observed in the overall ξ vs. $\kappa\mu_o$ pattern. In contrast, for $z_{ML}(=z_L)$=-1 this (local) maximum is by far lesser pronounced and it leads only to a modulation of the rate of decrease of ξ with increasing $\kappa\mu_o$. In addition, the foot of the aforementioned maxima is clearly shifted to lower $\kappa\mu_o$ as $z_{ML}(=z_L)$ becomes more negative. These findings are explained by the significant exclusion of L species from the electric Debye layer when $z_{ML}(=z_L)$ becomes negative, and by the ensuing dependence of the (equilibrium, §2.1) ligand concentration $c_L^{(e)}(r)=c_L^*\beta_L(r)$ on the position *r* from the particle surface to the bulk electrolyte, with $\beta_L(r)$ the L Boltzmann factor at *r*. For sufficiently large values of $|z_{ML}(=z_L)|$ (e.g. $z_{ML}(=z_L)$=-3 in **Figure 5A**) and large $1/\kappa$ (i.e. low $\kappa\mu_o$), the ligand concentration that is effectively operational in the reaction layer (denoted hereafter as $c_{L,eff}^*$) is necessarily close to 0 due to electrostatic exclusion of L from the electric double layer. Consequently, the corrected Damköhler number

$\bar{\kappa}_{a,eff} = \bar{\kappa}_a c^*_{L,eff} / c^*_L$ also approaches 0, which corresponds to complete nonlability of ML and a resulting $\xi \to 0$. When reducing $1/\kappa$ (or increasing μ_o), $c^*_{L,eff}$ necessarily increases (due to less repulsion and thus less electrostatic exclusion of L) and, therewith, $\bar{\kappa}_{a,eff}$ and the lability index ξ. At sufficiently large $\kappa\mu_o$ where the reaction layer extends significantly away from the Debye layer, we have $c^*_{L,eff} \to c^*_L$ and $\bar{\kappa}_{a,eff} \to \bar{\kappa}_a$, and ξ decreases with $\kappa\mu_o$ according to the conventional kinetic regime specified above for $y_a = 0$ (nonlabile ML case). In turn, these elements explain the origin of the (local) maximum observed for the dependence of ξ on $\kappa\mu_o$. Obviously, the significance of the position-dependent ligand concentration in determining ξ is tied to the magnitude of $|z_{ML}(=z_L)|$, which in turn defines the height and position of the maximum in ξ when varying $\kappa\mu_o$. **Figure 5B** illustrates that not only L but also ML is expelled from the reactive interface, in agreement with repulsive ML-particle electrostatics for $z_{ML}(=z_L) < 0$. The resulting ML depletion at the particle/medium interface generates therein a reduction in $\bar{c}_M$, albeit to lesser extent due to favorable M-particle attraction (**Figure 5C**). For the sake of completeness, we report in **SM** (**Figure S4**) the equivalent of **Figure 5** for the case of positively charged particles ($y_a = 2$). Qualitatively, the results basically mirror those discussed above for negative y_a, and maxima in $\bar{c}_M(r)$ close to the particle surface are very well identified for negatively charged ML (and L). Under the conditions prevailing in **Figure S4**, the transport of negatively charged ML to the particle surface and the ML surface concentration enhancement are facilitated by electrostatics, which in turn increases the M flux at the particle surface (see further discussion in §3.2.2). In other words, lability is promoted by negative ML charge that bypasses the repulsive M-particle interaction which, if solely operative, would lead to decreasing ML lability index (cf. **Figure 2A**).

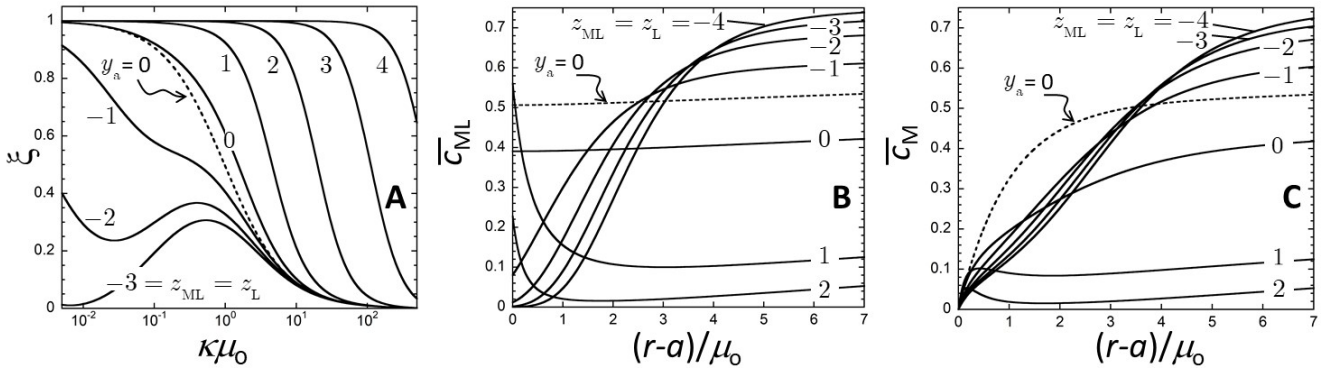

Figure 5. Dependence of ξ on $z_{ML} = z_L$ (indicated) as a function of $\kappa\mu_o$ (**A**). Corresponding $\bar{c}_{ML}(r)$ (**B**) and $\bar{c}_M(r)$ (**C**) profiles for $\kappa\mu_o = 1$. Adopted model parameters are $1/\kappa = 10$ nm, $y_a = -2$, $a = 1$ μm, $r_c/a = 50$, $\varepsilon = 1$, $\bar{K}_{ML} = 10^2$, $z_M = 2$. The dotted lines in (**A**)-(**C**) specify the situation for uncharged particles ($y_a = 0$).

3.2.2. Case of significant neutralization of ligand charges by metal ions ($z_{ML} = z_L + z_M$).

This situation corresponds to the intricate case where M, ML and L species are charged and the net charge of the ML complex is mediated by the only pairing of L with M. **Figure 6A** reports the ML lability index ξ as a function of y_a for different settings of $z_L = z_{ML} - z_M$ (with $z_M = 2$) at $\kappa\mu_o = 1$. Associated spatial distributions of

M and ML concentration profiles are provided in **Figures 6B-6E** for $y_a = -2$ and $y_a = 2$. Under the conditions adopted in **Figure 6**, the uncharged particle case corresponds to $\xi \approx 0.5$. This value of the ML lability index defines a common intersection point at $y_a = 0$ for all ξ vs. y_a curves generated for different $z_L = z_{ML} - z_M$ as, then, the impact of electrostatics on ξ at this point becomes irrelevant, regardless of $z_{i=M,L,ML}$. For $z_L = 1,\ldots,4$, species L and ML (and M) are all positively charged. In turn, ξ increases from 0.5 to unity with increasingly negative y_a due to attractive electrostatics. Qualitatively, the situation combines some of the features discussed in **Figure 2A** (uncharged ML and L) and **Figure 5A** (equally charged ML and L) with here distinct contributions of z_L and z_{ML} to the gain in ML lability. In agreement with **Figure 5A**, the more positive is z_L the steeper becomes the increase in ξ with decreasing y_a (< 0). When y_a is made increasingly positive, ξ progressively decreases, and for a given positive y_a, ξ decreases with increasingly positive z_L. These latter trends are due to enhanced repulsive particle electrostatics which mirror those discussed for $y_a < 0$.

The tested negative charges of L (blue curves in **Figure 6A**) with $z_L = -1,\ldots,-4$ encompass the peculiar situation where the sign of ML charge changes, with $z_{ML} = 1, \ldots,-2$. Despite this reversal of the ML charge, the ML lability index ξ decreases (increases) continuously at fixed $y_a < 0$ ($y_a > 0$) while making z_L more negative. This implies that the electrostatic effects connected to the L charge and to the dependence of its interfacial concentration on position predominantly determine the change in ML lability along the lines we detailed in §3.2.1. Closer inspection of **Figure 6A** reveals that ξ decreases with increasing y_a from negative to positive values at fixed $z_L = -1$ (i.e. $z_{ML} = 1$) whereas an opposite trend is observed for $z_L = -2,\ldots,-4$ (i.e. $z_{ML} = 0,\ldots,-2$). This is due to the differentiated contributions of the ML and L charges to the ML lability index depending on their attractive or repulsive interactions with the particle surface under the selected y_a and $\kappa\mu_o$ conditions. Full ML lability is further reached for significant L-particle attractive interactions. Briefly, the M and ML concentrations profiles given in **Figures 6B-6C** ($y_a < 0$) and **Figures 6D-6E** ($y_a > 0$) share common patterns with those provided in **Figures 5B-5C** and **Figures S4B-S4C** for the $z_{ML} = z_L$ configuration, respectively. Differences (e.g. in the amplitude of local maxima or in surface concentrations) are connected to the applicable value of z_{ML}.

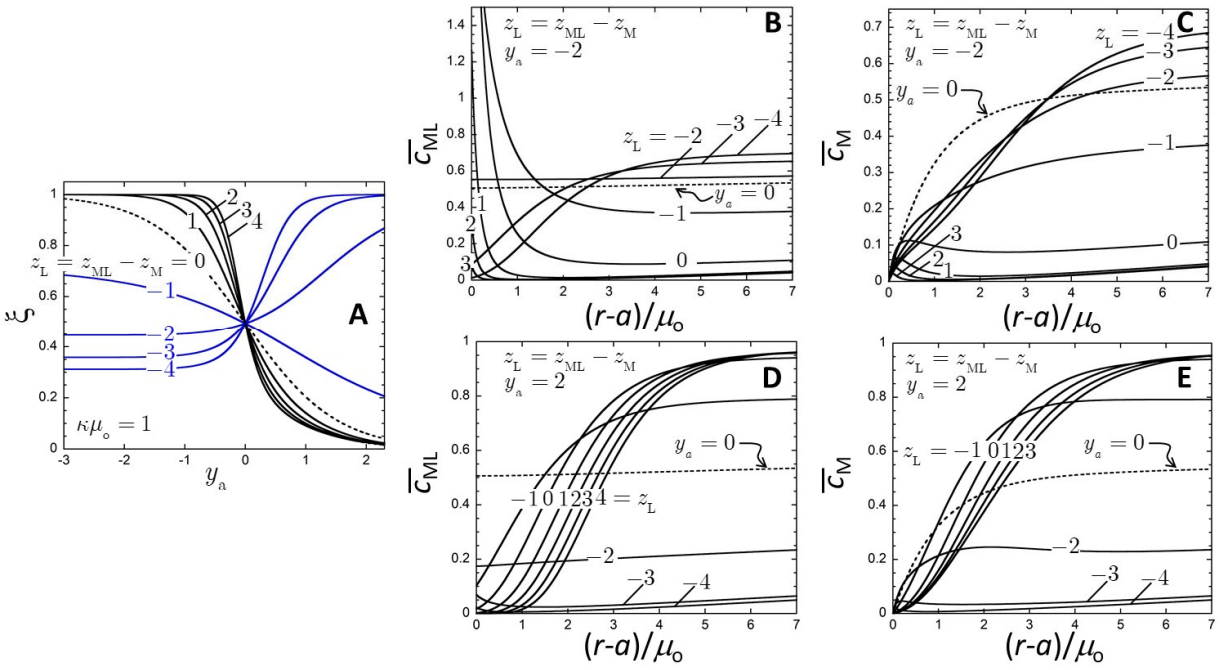

Figure 6. Dependence of ξ on $z_L = z_{ML} - z_M$ (indicated) plotted as a function of y_a for $\kappa\mu_o = 1$ (**A**). For readability purposes, blue and black solid curves highlight cases where L charge is negative and positive, respectively. Corresponding $\overline{c}_{ML}(r)$ (**B,D**) and $\overline{c}_M(r)$ (**C,E**) profiles for y_a = -2 (**B,C**) and $y_a = 2$ (**D,E**), as indicated. The dotted line in (**A**) specifies the situation for uncharged L ($z_L = 0$), and dotted lines in (**B**)-(**E**) correspond to the situation of uncharged particles ($y_a = 0$). Other adopted model parameters: $1/\kappa = 10$ nm, $a = 1$ μm, $r_c/a = 50$, $\varepsilon = 1$, $\overline{K}_{ML} = 10^2$, $z_M = 2$.

Finally, we illustrate in **Figure 7** how the M-surface flux $J_M(r=a) = J_M^{(a)}$ (Eq. (9) taken at $r = a$) varies with $\kappa\mu_o$ for various values of y_a at fixed $z_L = z_{ML}$ = -2 and 2 (**Figures 7A-7B**), and for various $z_L = z_{ML} - z_M$ at fixed y_a = -2 and 2 (**Figures 7C-7D**). Results are given in the dimensionless form $\overline{J}_M^{(a)} = J_M^{(a)} / J_M^{(a)}\big|_{y_a=0}$ (black solid curves) to ease comparison with predictions for the uncharged particle case. To further facilitate the interpretation of the nature of the flux (i.e. diffusive versus kinetic contribution, cf. Eqs (4)-(6)), for each condition tested we report the results in the forms $\overline{J}_M^{(a)} = J_M^{(a)} / J_M^{(a),dif}\big|_{y_a=0}$ (blue dotted lines) and $\overline{J}_M^{(a)} = J_M^{(a)} / J_M^{(a),kin}\big|_{y_a=0}$ (red dotted lines) where $J_M^{(a),dif}\big|_{y_a=0}$ is defined by Eq. (4) (with $\overline{\delta} >> a$ therein) and $J_M^{(a),kin}\big|_{y_a=0}$ by $J_M^{(a),kin}\big|_{y_a=0} = D_M c_M^* / a + k_d c_{ML}^* \mu_o$, as demonstrated in §2.2.2. Within the scope of the current study, it is important to discuss explicitly the variations of M flux at the reactive (bio)particle surface as a function of the dimensionless parameter $\kappa\mu_o$ because metal flux is a central quantity in the evaluation and interpretation of the ML lability index (Eq. (14)) and ML lability parameter (Eq. (3)). Accordingly, **Figure 7** below makes for the first time the connection between metal flux, lability index and nature of the process (i.e. ML dissociation kinetics or M/ML diffusion transports) that limits metal (bio)accumulation over time depending on the magnitude of the relevant electrostatic descriptors of M, L and ML (i.e. their respective valence), and those of the bioparticle surface (i.e. the surface potential y_a).

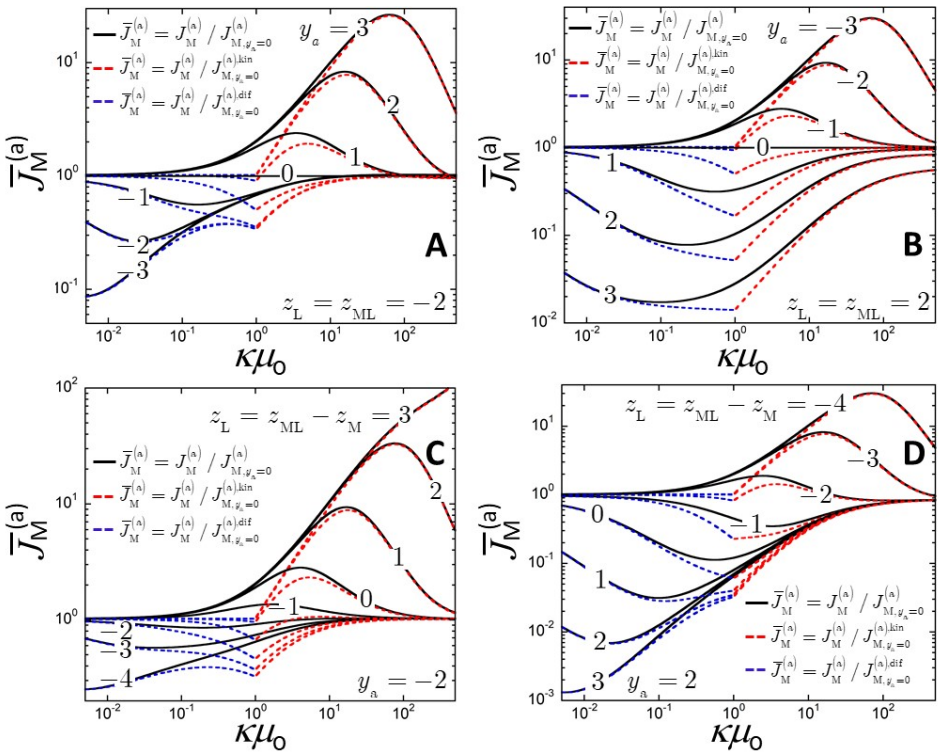

Figure 7. Evolution of the M surface flux $J_M(r=a)=J_M^{(a)}$ with $\kappa\mu_o$ as obtained from Eqs. (8)-(12), and normalized by $J_M^{(a)}\big|_{y_a=0}$ (solid black curves), $J_M^{(a),dif}\big|_{y_a=0}$ (blue dotted lines) and $J_M^{(a),kin}\big|_{y_a=0}$ (red dotted lines) where $J_M^{(a),dif}\big|_{y_a=0}$ and $J_M^{(a),kin}\big|_{y_a=0}$ are defined in the main text. Panels (**A**) to (**D**) refer to different settings of the particle surface potential y_a (indicated) and $z_{i=L,ML}$ (indicated). Other adopted model parameters: $1/\kappa = 10$ nm, $a = 1$ μm, $r_c/a = 50$, $\varepsilon = 1$, $\bar{K}_{ML} = 10^2$, $z_M = 2$.

The overall shape of the $\bar{J}_M^{(a)}$ versus $\kappa\mu_o$ plots is reminiscent of that discussed earlier for the dependence of ξ/ξ_o on the particle surface potential y_a (**Figure 2D**), which strengthens the intimate connections existing between ML lability and the nature of the M accumulation flux at the surface of the reactive particle, as discussed in §2. Gain or loss of ML lability as compared to the reference situation $y_a = 0$ depends on the sign of the dominant L/ML/M-particle interactions and on the magnitude of $\kappa\mu_o$ (cf. e.g. **Figures 2,3,5**). In addition, fully labile and nonlabile limits as achieved at sufficiently small and large $\kappa\mu_o$ - previously argued to be independent of particle electrostatics - result in a maximum or minimum in the representation ξ/ξ_o versus $\kappa\mu_o$ depending on the sign of y_a (**Figures 2D-2F**). These findings also apply to the normalized flux of M at the particle surface, the existence of a maximum or minimum being connected to the attractive or repulsive M/L/ML-particle interactions that *predominantly* impact on ML lability (**Figure 6**). Regardless of $\kappa\mu_o$, we have $\bar{J}_M^{(a)} < 1$ for parameter settings in line with $sign(y_a \times z_L) > 0$ and, conversely, $\bar{J}_M^{(a)} > 1$ for $sign(y_a \times z_L) < 0$ (**Figures 7A-7B**). Exceptions include the specific case where ML and L carry charges of opposite sign (**Figures 7C-7D**) for which it is the sign of the product $y_a \times z_{ML}$ that governs that of $\bar{J}_M^{(a)} - 1$ (cf. **Figure 6**). Cases $\bar{J}_M^{(a)} < 1$ and $\bar{J}_M^{(a)} > 1$ refer to a loss and gain of lability ($\xi/\xi_o < 1$ and $\xi/\xi_o > 1$, respectively) as compared to the situation met for uncharged particles, due to enhanced repulsion and attraction,

respectively, prevailing between the particle surface and L and, to some lesser extent, ML. Accordingly, the M flux decreases or increases relative to that evaluated at $y_a = 0$ for any value of $\kappa\mu_o$, and this relative decrease or increase is most significant at $\kappa\mu_o < 1$ and $\kappa\mu_o > 1$ where the ML lability index at $y_a = 0$ is highest and lowest, respectively. In turn, the modulations of $\bar{J}_M^{(a)}$ illustrated in **Figure 7** at $\kappa\mu_o < 1$ and $\kappa\mu_o > 1$ mainly reflect how the limiting *diffusive* and *kinetic* contributions to $\bar{J}_M^{(a)}$, respectively (cf. blue and red dotted lines in **Figure 7**) are impacted by particle electrostatics and by the underlying changes in L, ML and M concentration polarizations at the particle/medium interface. Depending on z_L, z_{ML}, y_a and $\kappa\mu_o$, $J_M^{(a)}$ may be a factor 10 to 100 larger or lower as compared to that estimated when either particle charge is 0 or particle electrostatics is significantly screened. In the field of ecotoxicology where the reactive particle can be assimilated to a microorganism or an active M-responsive tissue (e.g. bacteria, microalgae or fish gills), electrostatics-induced variations in metal bioaccumulation fluxes may have dramatic implications, e.g. cell death following an overshoot (deficiency) of toxic (essential, respectively) metals at $\kappa\mu_o > 1$ ($\kappa\mu_o < 1$, respectively). This finding strongly advocates for a careful analysis of the way in which interfacial physicochemical kinetics and transport processes at reactive (bio)surfaces are mediated by electrostatics so as to assess properly e.g. the impacts of ionic contaminants on biota. Current practice is however often reduced to simplistic thermodynamic considerations and adoption of Biotic Ligand Models where the operational coupling between reaction layer, diffusion layer and electric double layer is entirely ignored. Additional practical implications of this work are delineated in the following section.

4. Practical implications.

Evidently, the magnitude and nature of interfacial electric fields will play a crucial role in ion interaction kinetics across diverse domains such as mineral sorption, catalysis, electrokinetics, bioavailability/biouptake, etc. In each case, the effective interfacial electric field derives from the nature of the interface (hard/core shell/soft, density of structural charges) and its spatial scale, as well as the conditions in the medium, notably pH, ionic strength and background electrolyte composition. In the presence of an electric field, the local concentrations of ionic species (i.e. free M, ligand, H^+, background electrolyte ions) will differ from those in the bulk solution. It is these local conditions at the interface which determine the overall reactivity. Straightforward quantitative assessment of the applicability of our theory requires experimental systems for which the rate of the interfacial reaction can be measured as a function of the charge of the reactive surface, under conditions where chemical speciation in the exposure medium remains constant - or at least well defined. However, to the best of our knowledge no such systematic experimental data exist, and we therefore do not report here plots where experimental data are compared quantitatively to predictions from the theory formulated in this work. Instead, in the following we outline a few practical cases for which the effect of the interfacial electric field is qualitatively evident in line with expectations from theory.

Firstly, the rate of metal ion sorption on mineral surfaces is a useful practical example. The pH and electrolyte composition of the surrounding medium, together with the crystalline structure, determines the net surface charge carried by a mineral. Measurements of the rate of Cd(II) sorption on three minerals (sepiolite, palygorskite, and calcite) have been reported in the presence of several ligands at pH ca. 7 in 5 mM $CaCl_2$ electrolyte [56]. The point of zero charge (pzc) for sepiolite occurs at ca. pH 2 (in 1 mM KCl) [57], that for palygorskite at pH ca. 4 [58], and that for calcite at ca. pH 8 (in 1 mM KNO_3) [59]. Thus, at pH ca. 7 sepiolite will be negatively charged, palygorskite will also be negatively charged albeit to a lesser extent than sepiolite, whilst calcite will carry a positive surface charge. For the free Cd^{2+} alone, the sorption rate on sepiolite was observed to be greater than that of calcite [49]. This observation can be understood by extending Eq. (16) beyond the sink-condition in the context of M surface adsorption process, i.e. [48,49,60]

$$J_{\mathrm{M}}\left(r=a,t\right)=f_{\mathrm{el,M}}D_{\mathrm{M}}a^{-1}\left[c_{\mathrm{M}}^{*}-\beta_{\mathrm{M}}^{-1}\left(r=a\right)K_{\mathrm{H}}^{-1}\Gamma_{\mathrm{s}}\left(t\right)\right]=\mathrm{d}\Gamma_{\mathrm{s}}\left(t\right)/\mathrm{d}t \tag{32}$$

with $\Gamma_{\mathrm{s}}\left(t\right)$ (mol m^{-2}) the adsorbed metal concentration at time t and $K_{\mathrm{H}}^{-1}\Gamma_{\mathrm{s}}\left(t\right)=c_{\mathrm{M}}^{\mathrm{a}}$ is the surface concentration of M (uncorrected for electrostatics) in the linear adsorption regime (valid at sufficiently short t) with the chemical Henry adsorption coefficient denoted as K_{H} (m). Eq. (32) leads to

$$J_{\mathrm{M}}\left(r=a,t\right)=f_{\mathrm{el,M}}D_{\mathrm{M}}a^{-1}c_{\mathrm{M}}^{*}\mathrm{e}^{-\frac{f_{\mathrm{el,M}}D_{\mathrm{M}}a^{-1}}{\beta_{\mathrm{M}}\left(r=a\right)K_{\mathrm{H}}}t} \tag{33}$$

where $f_{\mathrm{el,M}}\approx 1$ for microparticles (cf. §2.2.1). Accordingly, from Eq. (33) we infer that the flux becomes increasingly greater as the surface charge becomes increasingly negative together with a corresponding increasing $\beta_{\mathrm{M}}\left(r=a\right)$ that well exceeds unity due to electrostatics-driven enhancement of M concentration at the particle surface. This trend agrees qualitatively with the experimental findings in [56]. However, the assessment of the potential ligand-assisted transfer of Cd(II) to the mineral surface requires analysis of the local concentration profiles of the involved species and the lability of the metal complexes. Insufficient experimental details were provided to enable such an analysis.

Metal bioavailability is another domain in which interfacial electric fields will influence the supply and uptake fluxes. In addition, biota themselves can actively modify the physicochemical conditions in the biointerfacial zone. For example, the pH near the surface of freshwater algae can be of the order of 1 pH unit higher than that in the bulk aqueous medium [61]. Such a difference in pH will have a large impact on the local metal speciation, and thus on the contributing supply and uptake fluxes. To date, a simplistic empirical equilibrium model has been used to interpret the consequences of this local pH environment for metal ion bioavailability, with the assumption that the equilibrium bulk concentration of the free metal ion is the only relevant species for biouptake [61,62]. However, such an assumption only holds if the rate of the interfacial uptake process is much slower than the rate of diffusive supply of free M towards the biointerface. Compliance with this kinetic criterion was not verified [61]. Rather, proper analysis of this situation requires coupling of the diffusive transport and lability of metal species in the exposure medium with biouptake kinetics in a dynamic type framework calling for implementation of Best equations [17,48,49,63].

In general, the pH and ionic strength in the interfacial region of a charged surface will differ from that in the bulk aqueous medium. Thus, during transport towards the reactive interface, the metal speciation dynamics will adapt to the local pH and electrolyte conditions as well as to the effective electric field. The interplay between the timescales of (de)protonation, ionic strength adaptation, and electrostatic relaxation will determine the overall interfacial reactivity. In this regard, we have presented earlier a framework for interpreting the chemical speciation dynamics in protonated system [64,65], which can be extended in the context of the theory presented therein.

5. Conclusions, and perspectives.

In this first exercise, we have illustrated the theoretical framework under limiting flux conditions, i.e. the situation where the reactive interface acts as a perfect sink for the target ion such as metal. However, the concepts are applicable to any metal boundary conditions, as supported by earlier demonstration that the lability of metal complexes is independent of the adopted interfacial boundary conditions [66]. Accordingly, in the case of metal-accumulating (bio)interfaces, the influence of the electrostatic field can be incorporated into Michaelis-Menten type descriptions of biouptake rates over the entire spectrum of metal bioaffinities and bioconversion capacities [17-20], thereby offering new insights into bioavailability-bioaccumulation relationships as well as strengthening quantitative interpretation of metal detection by whole-cell biosensors [41,67,68]. Via the analysis of different practical scenarios differing in terms of ML complex chemodynamics and biointerfacial electrostatics, the results detailed in this work emphasize the key importance of the coupling between electric double layers *and* reaction layers on the contribution of metal complexes to interfacial metal (bio)accumulation. Overall, dominating M/ML/L-particle repulsion and attraction may lead to significant loss and gain in metal complex lability as compared to the uncharged particle case, respectively. These changes are associated to here identified-modulations in the interfacial concentrations of the relevant metal species, as determined by intertwined chemical kinetic, diffusive and conductive processes.

The framework presented herein for molecular complexants can be extended to treat the case of nanoparticulate complexants. This situation is however somewhat more involved due to the necessary additional coupling between the local intraparticulate reaction layer and the reaction layer operational at the macroscopic metal-consuming interface [69-71]. On top of this, the treatment will require adequate implementation of the overlap between the electric double layer of the reactive macrosurface and that of the charged nanoparticulate complexant. Nevertheless, in principle it is possible to include the necessary electric field parameters within the existing Eigen-extended framework for describing the lability of nanoparticulate metal complexes [71]. Finally, we underscore that our conceptual framework holds for any system in which the transport of a charged analyte is assisted by other charged entities. It is thus envisaged to find broad conceptual applicability across diverse domains including catalysis, bioremediation, ecotoxicology, and drug delivery.

Main symbols and abbreviations

Latin

a	radius of the (spherical) consuming particle or interface (m)
c_L^*	concentration of free L in the bulk medium (mol m^{-3})
c_M	concentration of M (mol m^{-3}) (dimensionless form: $\overline{c}_M$)
c_{ML}	concentration of ML (mol m^{-3}) (dimensionless form: $\overline{c}_{ML}$)
$c_{M,t}^*$	total metal concentration in the bulk medium (mol m^{-3})
D_M	diffusion coefficient of M (m^2 s^{-1})
D_{ML}	diffusion coefficient of ML (m^2 s^{-1})
$f_{el,M}$	conductive coefficient for M diffusion (dimensionless)
J_{dif}	diffusive flux (mol m^{-2} s^{-1})
J_{kin}	kinetic flux (mol m^{-2} s^{-1})
k_a	association rate constant (m^3 mol^{-1} s^{-1})
k_d	dissociation rate constant (s^{-1})
K_{ML}	stability constant of ML (m^3 mol^{-1}) (dimensionless form: $\overline{K}_{ML}$)
L	free ligand
$\mathcal{L}$	lability parameter (dimensionless)
M	free metal ion
ML	metal complex
r	radial coordinate (dimensionless form $\overline{r}$).
y_a	dimensionless surface potential of the (spherical) M-consuming particle
$z_{i=L,M,ML}$	charge of L, M and ML

Greek

$\beta_{i=L,M,ML}(r)$	Boltzmann factor at position r for L, M and ML species.
$\overline{\delta}$	mean diffusion layer thickness (m)
ε	ratio between D_{ML} and D_M (dimensionless)
ξ	ML lability index (dimensionless)
$1/\kappa$	Debye screening length or characteristic electric double layer thickness (m)
$\overline{\kappa}_a$	dimensionless Damköhler number for the kinetics of association of M with L (uncharged particle case)
μ_o	reaction layer thickness for the case of uncharged particle (m)

CRediT authorship contribution statement

Jérôme F.L. Duval: Conceptualization, Methodology, Software, Formal analysis, Validation, Investigation, Writing – original draft. **H.P. van Leeuwen**: Investigation, Writing-Reviewing & Editing. **R.M. Town** Investigation, Writing-Reviewing & Editing.

Declaration of Competing Interest

The authors declare that they have no known competing financial interests or personal relationships that could have appeared to influence the work reported in this paper.

Data availability

Numerical codes and data will be made available on request.

Acknowledgements. RMT acknowledges financial support from the UAntwerpen SEP-BOF 2020 grant "From exposure to effects of pollutants: a dynamic mechanistic basis". JFLD acknowledges financial supports from French national program EC2CO (MENABIOL project) and from OTELO (Observatoire Terre Environnement Lorraine, Interdisciplinary AAP project 2020).

Supplementary material

I. Expressions of the constants $\alpha_{1,2}$ and $c_{1,2}$ involved in Eqs. (26), (27) and (30) of the main text. **II.** Supplementary Figures. M and ML concentration profiles for different values of y_a and $\bar{K}_{ML}$ with $z_{ML} = z_L = 0$ (**Fig. S1**). M and ML concentration profiles for different values of y_a and $\kappa\mu_o$ with $z_{ML} = z_L = 0$ (**Figs. S2-S3**). Dependence of the ML lability index ξ on $\kappa\mu_o$ for different values of $z_{ML} = z_L$, and corresponding M and ML concentrations profiles under selected $\kappa\mu_o$ condition (**Fig. S4**).

References

[1] H.P. van Leeuwen, R.M. Town, J. Buffle, R.F.M.J. Cleven, W. Davison, J. Puy, W.H. van Riemsdijk, L. Sigg, Dynamic speciation analysis and bioavailability of metals in aquatic systems, Environ. Sci. Technol. 39 (2005) 8545-8556.

[2] P.R. Paquin, J.W. Gorsuch, S. Apte, G.E. Batley, K.C. Bowles, P.G.C. Campbell, C.G. Delos, D.M. Di Toro, R.L. Dwyer, F. Galvez, R.W. Gensemer, G.G. Goss, C. Hogstrand, C.R. Janssen, J.C. McGeer, R.B. Naddy, R.C. Playle, R.C. Santore, U. Schneider, W.A. Stubblefield, C.M. Wood, K.B. Wu, The biotic ligand model: a historical overview. Comp. Biochem. Physiol. C 133 (2002) 3-35.

[3] C.S. Hassler, K.W. Wilkinson, Failure of the biotic ligand and free-ion activity models to explain zinc bioaccumulation by *Chlorella kesslerii,* Env. Tox. Chem. 22 (2003) 620-626.

[4] C. Anne, P.G.C. Campbell, C. Fortin, Biotic ligand model can successfully predict the uptake of a trivalent ion by a unicellular alga below pH 6.50 but not above: possible role of hydroxo-species, Env. Sci. Technol. 47 (2017) 2408-2415.

[5] J. Luo, H. Zhang, F.-J. Zhao, W. Davison, Distinguishing diffusional and plant control of Cd and Ni uptake by hyperaccumulator and nonhyperaccumulator plants, Env. Sci. Technol. 44 (2010), 6636-6641.

[6] F. Degryse, E. Smolders, R. Merckx, Labile Cd complexes increase Cd availability to Plants. Env. Sci. Technol. 40 (2006) 830-836.

[7] K.O. Yoro, M.K. Amosa, P.T. Sekoai, J. Mulopo, M.O. Daramola, Diffusion mechanism and effect of mass transfer limitation during the adsorption of CO_2 by polyaspartamide in a packed-bed unit, Intern. J. Sustainable Engin. 13 (2020) 54-67.

[8] D. Shen, M.B. Vukmirovic, R. Akolkar, Understanding the role of Complexation in the charge-transfer kinetics of the $Cu^{2+} + e^- \leftrightarrow Cu^{1+}$ redox reaction in ethaline deep eutectic solvent, J. Electrochem. Society 166 (2019) E526.

[9] J. Yin, J. Redovich, Kinetic modeling of virus growth in cells, Micro. Mol. Biol. Rev. 82 (2018) e00066-17.

[10] J.-W. Yoo, D.J. Irvine, D.E. Discher, S. Mitragotri, Bio-inspired, bioengineered and biomimetic drug delivery carriers, Nature Rev. Drug. Discovery 10 (2011) 521-535.

[11] H.P. van Leeuwen, Kinetic classification of metal complexes in electroanalytical speciation, J. Electroanal. Chem. 99 (1979) 93-102.

[12] V.G. Levich, Physicochemical Hydrodynamics, Prentice Hall, Englewood Cliffs, NJ, 1962.

[13] R. Brdička, K. Wiesner, K., Polarographic determination of the rate of the reaction between ferrohem and hydrogen peroxide, Collect. Czech. Chem. Commun. 12 (1947) 39-63.

[14] J. Koutecký, Theorie langsamer elektrodenreaktionen in der polarographie und polarographisches verhalten eines systems, bei welchem der depolarisator durch eine schnelle chemische reaction aus einem elektroinaktiven stoff entsteht, Collect. Czech. Chem. Commun. 18 (1953) 597-610.

[15] J. Heyrovský, J. Kůta, J., Principles of Polarography, Publishing House of the Czechoslovak Academy of Science, Praha and Academic Press, New York, 1966.

[16] Z. Zhang, J. Buffle, H.P. van Leeuwen, Roles of dynamic metal speciation and membrane permeability in metal flux through lipophilic membranes: general theory and experimental validation with nonlabile complexes, Langmuir 23 (2007) 5216-5226.

[17] H.P. van Leeuwen, Metal speciation dynamics and bioavailability: inert and labile complexes, Environ. Sci. Technol. 33 (1999) 3743-3748.

[18] H.P. van Leeuwen, Speciation dynamics and bioavailability of metals, J. Radioanal. Chem. 246 (2000) 487-492.

[19] S. Jansen, R. Blust, H.P. van Leeuwen, Metal speciation dynamics and bioavailability: Zn(II) and Cd(II) uptake by mussel (*Mytilus edilus*) and carp (*Cyprinus carpio*), Environ. Sci. Technol. 36 (2002) 2164-2170.
[20] R.M. Town, H.P. van Leeuwen, Chemodynamic features of nickel(II) and its complexes: implications for bioavailability in freshwaters, Ecotoxicol Environ. Safety 214 (2022) 113840.
[21] R. Zimmerman, J.F.L. Duval, C. Werner, On the analysis of ionic surface conduction to unravel charging processes at macroscopic soft and hard solid-liquid interfaces, Curr. Opin. Colloid Interface Sci. 44 (2019) 177-187.
[22] M. von Smoluchowski, in: L. Graetz (Ed.), Handbuch der Elektrizitat und des Magnetismus, vol. II, Barth, Leipzig, 1921, pp. 366–428.
[23] C. Werner, H. Körber, R. Zimmermann, S.S. Dukhin, H.J. Jacobasch, Extended electrokinetic characterization of flat solid surfaces, J. Colloid Interface Sci. 208 (1998) 329-346.
[24] J. Lyklema, Surface conduction, J. Phys.: Condens. Matter 13 (2001) 5027-5034.
[25] J. Lyklema, M. Minor, On surface conduction and its role in electrokinetics, Colloids Surf. A 140 (1998) 33-41.
[26] R. Zimmermann, S. Dukhin, C. Werner, Electrokinetic measurements reveal interfacial charge at polymer films caused by simple electrolyte ions, J. Phys. Chem. B 105 (2001) 8544-8549.
[27] P. Leroy, C. Tournassat, O. Bernard, N. Devau, M. Azaroual, The electrophoretic mobility of montmorillonite. Zeta potential and surface conductivity effects, J. Colloid Interface Sci. 451 (2015) 21-39.
[28] P.P. Gopmandal, J.F.L. Duval, Electrostatics and electrophoresis of engineered nanoparticles and particulate environmental contaminants: beyond zeta potential-based formulation, Curr. Opin. Colloid Interface Sci. 60 (2022) 101605.
[29] J.F.L. Duval, D. Kütner, M. Nitschke, C. Werner, R. Zimmermann, Interrelations between charging, structure and electrokinetics of nanometric polyelectrolyte films, J. Colloid Interface Sci. 362 (2011) 439-449.
[30] R. Zimmermann, G. Gunkel-Grabole, J. Bünsow, C. Werner, W.T.S. Huck, J.F.L. Duval, Evidence of ion-pairing in cationic brushes from evaluation of brush charging and structure by electrokinetic and surface conductivity analysis, J. Phys. Chem. C 121 (2017) 2915-2922.
[31] R. Zimmermann, D. Romeis, I. Bihannic, M. Cohen-Stuart, J.-U. Sommer, C. Werner, J.F.L. Duval, Electrokinetics as an alternative to neutron reflectivity for evaluation of segment density distribution in PEO brushes, Soft Matter 10 (2014) 7804-7809.
[32] R. Zimmermann, S.S. Dukhin, C. Werner, J.F.L. Duval, On the use of electrokinetics for unraveling charging and structure of soft planar polymer films, Curr. Opin. Colloid Interface Sci. 18 (2013) 83-92.
[33] J.F.L. Duval, F. Gaboriaud, Progress in electrohydrodynamics of soft microbial particle interphases, Curr. Opin. Colloid Interface Sci. 15 (2010) 184-195.
[34] C. Pagnout, R.M. Présent, P. Billard, E. Rotureau, J.F.L. Duval, What do luminescent bacterial metal-sensors probe? Insights from confrontation between experiments and flux-based theory, Sens. Actuators B Chem. 270 (2018) 482-491.
[35] C. Dika, C. Gantzer, A. Perrin, J.F.L. Duval, Impact of the virus purification protocol on aggregation and electrokinetics of MS2 phage and corresponding virus-like particles, Phys. Chem. Chem. Phys. 15 (2013) 5691-5700.
[36] C. Dika, J.F.L. Duval, H.M. Ly, C. Merlin C., C. Gantzer, Impact of internal RNA on aggregation and electrokinetics of viruses: comparison between MS2 phage and corresponding virus-like-particles, Appl. Environ. Microbiol. 77 (2011) 4939-4948.
[37] J. Langlet, F. Gaboriaud, C. Gantzer, J.F.L. Duval, Impact of chemical and structural anisotropy on the electrophoretic mobility of spherical soft-multilayer particles: the case of bacteriophage MS2, Biophys. J. 94 (2008) 3293-3312.
[38] H.P. van Leeuwen, J. Buffle, J.F.L. Duval, R.M. Town, Understanding the extraordinary ionic reactivity of aqueous nanoparticles, Langmuir 29 (2013) 10297-10302.
[39] H.P. van Leeuwen, J.F.L. Duval, J.P. Pinheiro, R. Blust, R.M. Town, Chemodynamics and bioavailability of metal ion complexes with nanoparticles in aqueous media, Environ. Sci.: Nano 4 (2017) 2108-2133.

[40] F. Gaboriaud, E. Dague, S. Bailet, F. Jorand, J. Duval, F. Thomas, Multiscale dynamics of the cell envelope of Shewanella putrefaciens as a response to pH change, Colloids Surf. B Biointerfaces 52 (2006) 108-116.
[41] J.F.L. Duval, C. Pagnout, Decoding the time-dependent response of bioluminescent metal-detecting whole-cell bacterial sensors. *ACS Sensors* 4 (2019) 1373-1383.
[42] E. Vouriot, I. Bihannic, A. Beaussart, Y. Waldvogel, A. Razafitianamaharavo, T. Ribeiro, J.P.S. Farinha, C; Beloin, J.F.L. Duval, Electrophoresis as a simple method to detect deleterious actions of engineered nanoparticles on living cells, Environ. Chem. 17 (2019) 39-53.
[43] J.F.L. Duval, H.P. van Leeuwen, W. Norde, R.M. Town, Chemodynamic features of nanoparticles: application to understanding the dynamic life cycles of SARS-CoV-2 in aerosols and aqueous biointerfacial zones, Adv. Colloid Interface Sci. 290 (2021) 102400.
[44] H. Nguyen, P.D. Lan, D.A. Nissley, E.P. O'Brien, M.S. Li, Electrostatic interactions explain the higher binding affinity of the CR3022 antibody for SARS-CoV-2 than the 4A8 antibody, J Phys. Chem. B 125 (2021) 7368-7379.
[45] S.S. Goher, F. Ali, M. Amin, The Delta variant mutations in the receptor binding domain of SARS-CoV-2 show enhanced electrostatic interactions with ACE2, Med. Drug Discovery 13 (2022) 100114.
[46] M. Eigen, Fast elementary steps in chemical reaction mechanisms. Pure Appl. Chem. 6 (1963) 97−115.
[47] R.M. Fuoss, Ionic Association. III. The equilibrium between ion pairs and free Ions. J. Am. Chem. Soc. 80 (1958) 5059−5061.
[48] J.F.L. Duval, Dynamics of metal uptake by charged biointerphases: bioavailability and bulk depletion, Phys. Chem. Chem. Phys. 15 (2013) 7873-7888.
[49] J.F.L. Duval, E. Rotureau, Dynamics of metal uptake by charged soft biointerphases: impacts of depletion, internalisation, adsorption and excretion, Phys. Chem. Chem. Phys. 16 (2014) 7401-7416.
[50] J.P. Pinheiro, J. Galceran, H.P. van Leeuwen, Metal speciation dynamics and bioavailability: bulk depletion effects, Environ. Sci. Technol. 38 (2004) 2397-2405.
[51] Z. Chen, R.K. Singh, General solution for Poisson-Boltzmann equation in semiinfinite planar symmetry, J. Colloid Int. Sci. 245 (2002) 301-306.
[52] H.P. van Leeuwen, J. Puy, J. Galceran, J. Cecilia, Evaluation of the Koutecký-Koryta approximation for voltammetric currents generated by metal complex systems with various labilities. J. Electroanal. Chem. 526 (2002) 10-18.
[53] J. Galceran, J. Puy, J. Salvador, J. Cecilia, H.P. van Leeuwen, Voltammetric lability of metal complexes at spherical microelectrodes with various radii, J. Electroanal. Chem. 505 (2001) 85-94.
[54] U. Ascher, J. Christiansen, R. D. Russel, Collocation software for boundary-value ODEs, ACM Trans. Math. Software 7 (1981) 209-222.
[55] J.F.L. Duval, H.P. van Leeuwen, Rates of ionic reactions with charged nanoparticles in aqueous media, J. Phys. Chem. A 116 (2012) 6443-6451.
[56] M. Shirvani, H. Shariatmadari, M. Kalbasi, F. Nourbakhsh, B. Najafi, Sorption of cadmium on palygorskite, sepiolite and calcite: equilibria and organic ligand affected kinetics, Colloid Surf. A 287 (2006) 182-190.
[57] C. Knapp, F.J. Gil-Llambías, M. Gulppi-Cabra, P. Avila, J. Blanco, Phase distribution in titania-sepiolite catalyst supports prepared by different methods, J. Mater. Chem. 7 (1997) 1641-1645.
[58] A. Neaman, A. Singer, Rheological properties of aqueous suspensions of palygorskite, Soil Sci. Soc. Am. J. 64 (2000) 427-436.
[59] M. Kosmulski, The pH dependent surface charging and points of zero charge. VII. Update, Adv. Colloid Interface Sci. 251 (2018) 115-138.
[60] J. Galceran, H.P. van Leeuwen, Dynamics of biouptake processes: the role of transport, adsorption and internalisation. In *Physicochemical kinetics and transport at biointerfaces*, eds. H.P. van Leeuwen and W. Köstler, J. Wiley & Sons 2004, West Sussex, Chapter 4, p. 172.
[61] F. Liu, Q.-G. Tan, D. Weiss, A. Crémazy, C. Fortin, P.G.C. Campbell, Unravelling metal speciation in the microenvironment surrounding phytoplankton cells to improve predictions of metal bioavailability, Environ. Sci. Technol. 54 (2020) 8177-8185.

[62] M. Lavoie, J.F.L. Duval, J.A. Raven, F. Maps, B. Bejaoui, D.J. Kieber, W.F. Vincent, Carbonate disequilibrium in the external boundary layer of freshwater chrysophytes: implications for contaminant uptake, Environ. Sci. & Technol. 52 (2018) 9403-9411.
[63] H.P. van Leeuwen, Speciation dynamics and bioavailability of metals. J. Radioanal. Nucl. Chem. 246 (2000) 487-492.
[64] H.P. van Leeuwen, R.M. Town, J. Buffle, Impact of ligand protonation on Eigen-type metal complexation kinetics in aqueous systems. J. Phys. Chem. A 111 (2007) 2115-2121.
[65] H.P. van Leeuwen, R.M. Town, Impact of ligand protonation on higher-order metal complexation kinetics in aqueous systems, J. Phys. Chem. A 112 (2008) 2563-2571.
[66] Z. Zhang, D. Alemani, J. Buffle, R.M. Town, K.J. Wilkinson, Metal flux through consuming interfaces in ligand mixtures: boundary conditions do not influence lability and relative contributions of metal species, Phys. Chem. Chem. Phys. 13 (2011) 17606-17614.
[67] E. Delatour, C. Pagnout, M. Zaffino, J.F.L. Duval, Exploiting catabolite repression and stringent response to control delay and multimodality of bioluminescence signal by metal whole-cell biosensors: interplay between metal bioavailability and nutritional medium conditions, Biosensors 12 (2022) 327.
[68] E. Delatour, C. Pagnout, M. Zaffino, J.F.L. Duval, Comparative analysis of cell metabolic activity sensing by Escherichia coli rrnB P1-lux and Cd responsive-lux biosensors: time-resolved experiments and mechanistic modelling, Biosensors 12 (2022) 763.
[69] H.P. van Leeuwen, R.M. Town, Lability of nanoparticulate metal complexes in electrochemical speciation analysis, J. Solid State Electrochem 20 (2016) 3255-3262.
[70] J.F.L. Duval, R.M. Town, H.P. van Leeuwen, Applicability of the reaction layer principle to nanoparticulate metal complexes at a macroscopic reactive (bio)interface: a theoretical study, J. Phys. Chem. C 121 (2017) 19147-19161.
[71] J.F.L. Duval, R.M. Town, H.P. van Leeuwen, Lability of nanoparticulate metal complexes at a macroscopic metal responsive (bio)interface: expression and asymptotic scaling laws, J. Phys. Chem. C 122 (2018) 6052-6065.

Figure Captions.

Figure 1. Schematic representation of the transport, chemical kinetic and electrostatic contributions to the overall flux of metal ions (M) at an electrically charged interface (e.g. organism or electrode) that consumes free M. The valences of species M, ML and L are denoted as z_M, z_{ML} and z_L, respectively, and the diffusion layer thickness is set to a, the curvature radius of the consuming interface. The work aims at addressing the effects of electrostatics on the lability of ML complex and, therewith, the way the interplay between reaction layer, electric double layer and diffusion layer affects the overall transfer of M to the reactive surface. The electrostatic factors $\beta_{i=L,M,ML}$ and $f_{el,i=L,M,ML}$ refer to the Boltzmann accumulation/depletion and conductive acceleration/retardation of diffusion for L, M and ML species, respectively. See text for details.

Figure 2. Dependence of ML lability index ξ on y_a (indicated) (**A**), and on $\overline{K}_{ML}$ (**B**) and $\varepsilon = D_{ML} / D_M$ (**C**) for y_a = -2, 0 and 2 (indicated), as a function of $\kappa\mu_o$. In (**B**): $\overline{K}_{ML} = 10$ (a), 10^2 (b), 10^3 (c). In (**C**): $\varepsilon = 0.1$ (a), 1 (b). Dotted lines in (**A**) and (**B**)-(**C**) refer to the uncharged particle case (Eq. (23)) and to the kinetic limit $\xi \to \overline{\kappa}_a^{1/2} / \left(\varepsilon \overline{K}_{ML}\right)$, respectively. Panels (**D**), (**E**) and (**F**) report (and extend) results of (**A**), (**B**) and (**C**) in the form ξ / ξ_o where ξ_o is the ML lability index at $y_a = 0$. Dotted lines in (**D**)-(**F**) are predictions using the linearized Debye-Hückel (denoted as 'D-H') expression of $y(r)$ (Eq. (13)). (**A**)-(**F**): solid lines refer to results from numerical solving of Eqs. (8), (10)-(12)/(13), (14). Unless otherwise specified, adopted model parameters are: $1/\kappa = 10$ nm, $a = 1$ μm, $r_c / a = 50$, $\varepsilon = 1$, $\overline{K}_{ML} = 10^2$, $z_M = 2$, $z_{ML} = z_L = 0$.

Figure 3. (A) Dependence of ξ on y_a (indicated) and κ^{-1} as a function of $\kappa\mu_o$. $1/\kappa = 1$ nm (a), 10 nm (b), 30 nm (c). (**B**) As in (**A**) for ξ / ξ_o. Dotted lines in (**A**) and (**B**) refer to the kinetic limit $\xi \to \overline{\kappa}_a^{1/2} / \left(\varepsilon \overline{K}_{ML}\right)$ and to predictions with linearized Debye-Hückel (D-H) expression of $y(r)$ (Eq. (13)), respectively. (**C**) ξ / ξ_o versus y_a for different $\kappa\mu_o$ (indicated) and $1/\kappa = 10$ nm. (**D**) ξ / ξ_o versus y_a for $1/\kappa = 1$ nm (a), 10 nm (b), 30 nm (c) and $\kappa\mu_o = 10$. Black and colored dotted lines in (**C**) and (**D**) refer to predictions within D-H framework and with using Eq. (30), respectively. (**A**)-

(**D**): colored solid lines are results from numerical solving of Eqs. (8), (10)-(12)/(13), (14). Unless otherwise specified, model parameters are: $1/\kappa = 10$ nm, $a = 1$ μm, $r_c/a = 50$, $\varepsilon = 1$, $\overline{K}_{ML} = 10^2$, $z_M = 2$, $z_{ML} = z_L = 0$.

Figure 4. Spatial distributions of the concentration profiles $\overline{c}_M(r) = c_M(r)/c_M^*$ (dotted lines) and $\overline{c}_{ML}(r) = c_{ML}(r)/c_{ML}^*$ (solid lines) for $y_a = -2$ (**A**), 0 (**B**) and 2 (**C**) plotted as a function of the scaled space variable $(r-a)/\mu_o$ for $\kappa\mu_o = 10$ (blue), 1 (red) and 10^{-2} (black). Dotted and solid black curves for $\overline{c}_M(r)$ and $\overline{c}_{ML}(r)$, respectively, are confounded for $\kappa\mu_o = 10^{-2}$ (this is the fully labile limit, $\xi \to 1$). Adopted model parameters are $1/\kappa = 10$ nm, $a = 1$ μm, $r_c/a = 50$, $\varepsilon = 1$, $\overline{K}_{ML} = 10^2$, $z_M = 2$, $z_{ML} = z_L = 0$. The Debye layer region of thickness κ^{-1} is indicated in panel (**A**) for the three $\kappa\mu_o$ -conditions examined.

Figure 5. Dependence of ξ on $z_{ML} = z_L$ (indicated) as a function of $\kappa\mu_o$ (**A**). Corresponding $\overline{c}_{ML}(r)$ (**B**) and $\overline{c}_M(r)$ (**C**) profiles for $\kappa\mu_o = 1$. Adopted model parameters are $1/\kappa = 10$ nm, $y_a = -2$, $a = 1$ μm, $r_c/a = 50$, $\varepsilon = 1$, $\overline{K}_{ML} = 10^2$, $z_M = 2$. The dotted lines in (**A**)-(**C**) specify the situation for uncharged particles ($y_a = 0$).

Figure 6. Dependence of ξ on $z_L = z_{ML} - z_M$ (indicated) plotted as a function of y_a for $\kappa\mu_o = 1$ (**A**). For readability purposes, blue and black solid curves highlight cases where L charge is negative and positive, respectively. Corresponding $\overline{c}_{ML}(r)$ (**B,D**) and $\overline{c}_M(r)$ (**C,E**) profiles for $y_a = -2$ (**B,C**) and $y_a = 2$ (**D,E**), as indicated. The dotted line in (**A**) specifies the situation for uncharged L ($z_L = 0$), and dotted lines in (**B**)-(**E**) correspond to the situation of uncharged particles ($y_a = 0$). Other adopted model parameters: $1/\kappa = 10$ nm, $a = 1$ μm, $r_c/a = 50$, $\varepsilon = 1$, $\overline{K}_{ML} = 10^2$, $z_M = 2$.

Figure 7. Evolution of the M surface flux $J_M(r=a) = J_M^{(a)}$ with $\kappa\mu_o$ as obtained from Eqs. (8)-(12), and normalized by $J_M^{(a)}\big|_{y_a=0}$ (solid black curves), $J_M^{(a),dif}\big|_{y_a=0}$ (blue dotted lines) and $J_M^{(a),kin}\big|_{y_a=0}$ (red dotted lines) where $J_M^{(a),dif}\big|_{y_a=0}$ and $J_M^{(a),kin}\big|_{y_a=0}$ are defined in the main text. Panels (**A**) to (**D**) refer to different settings of the particle surface potential y_a (indicated) and $z_{i=L,ML}$ (indicated). Other adopted model parameters: $1/\kappa = 10$ nm, $a = 1$ μm, $r_c/a = 50$, $\varepsilon = 1$, $\overline{K}_{ML} = 10^2$, $z_M = 2$.

SUPPLEMENTARY MATERIAL

Electrostatic effects on ligand-assisted transfer of metals to (bio)accumulating interfaces and metal complexes (bioavai)lability.

Jérôme F. L. Duval [a,*], Herman P. van Leeuwen [b,c], Raewyn M. Town [c]

[a] Université de Lorraine, CNRS, LIEC, F-54000 Nancy, France. E-mail address: jerome.duval@univ-lorraine.fr
[b] Physical Chemistry and Soft Matter, Wageningen University & Research, Stippeneng 4, 6708 WE Wageningen, The Netherlands
[c] ECOSPHERE, Department of Biology, Universiteit Antwerpen, Groenenborgerlaan 171, 2020 Antwerpen, Belgium

This document contains 6 pages, 20 equations and 4 Supplementary Figures.

I. Expressions of the constants $\alpha_{1,2}$ and $c_{1,2}$ involved in Eqs. (26), (27) and (30) of the main text.

The constants $\alpha_{1,2}$ and $c_{1,2}$ defining M and ML concentration profiles under the conditions examined in §2.2.3 (i.e. $z_{ML}=0$, $\kappa\mu_o >> 1$, and Debye-Hückel formulation of the potential distribution $y(r)$, cf. Eq. (13)) are defined by the boundaries expressed by Eqs. (10)-(11) taken in the limit $z_{ML}=0$. In terms of $\overline{c}_{i=M,ML}$, these boundaries become

$$\begin{cases} \overline{c}_M(r=a)=0 \quad \text{(a)} \\ \mathrm{d}\overline{c}_{ML}(r)/\mathrm{d}r\big|_{r=a}=0 \quad \text{(b)} \\ \overline{c}_{i=M,ML}(r=r_c)=1 \quad \text{(c)} \end{cases} \tag{S1}$$

To lighten notations, we proceed to the evaluation of $\alpha_{1,2}$ and $c_{1,2}$ first for the case $y_a>0$, and then for $y_a<0$.

a. Case of (strictly) positive surface potential $y_a>0$***.*** Combining Eq. (S1a) with Eqs. (26)-(27), we obtain

$$-c_1+a^{-1}\varepsilon\overline{K}_{ML}\left(\alpha_1 J_\lambda^a+\alpha_2 Y_\lambda^a\right)=0 \tag{S2}$$

, where we introduced $J_\lambda^a=J_\lambda(\overline{X}_a)$, $Y_\lambda^a=Y_\lambda(\overline{X}_a)$ with $\overline{X}_a=\overline{X}_{r=a}$. After some algebra, Eq. (S1b) leads to

$$-\beta_M^a c_1+\theta_a\left(\alpha_1 \mathrm{d}J_\lambda^a+\alpha_2 \mathrm{d}Y_\lambda^a\right)=0 \tag{S3}$$

, with $\theta_a=2^{-1}\varepsilon\overline{K}_{ML}\kappa\beta_M^a\overline{X}_a$ (m^{-1}), $\mathrm{d}J_\lambda^a=-\lambda_a J_\lambda^a+J_{\lambda+1}^a$, $\mathrm{d}Y_\lambda^a=-\lambda_a Y_\lambda^a+Y_{\lambda+1}^a$ and $\lambda_a=\lambda/\overline{X}_a$ (dimensionless). Combining Eq. (27) with Eq. (S1c) specified for i=ML yields

$$-r_c+\alpha_1 J_\lambda^c+\alpha_2 Y_\lambda^c+c_1 I_1^c+c_2 I_2^c=0 \tag{S4}$$

with $J_\lambda^{\mathrm{c}} = J_\lambda\left(\bar{X}_{\mathrm{c}}\right)$, $Y_\lambda^{\mathrm{c}} = Y_\lambda\left(\bar{X}_{\mathrm{c}}\right)$ and $\bar{X}_{\mathrm{c}} = \bar{X}_{r=r_{\mathrm{c}}}$, and we introduced the integral terms I_1^{c} (in m) and I_2^{c} (dimensionless) defined by

$$\begin{cases} I_1^{\mathrm{c}} = \pi\dfrac{\gamma}{\kappa}\left\{ Y_\lambda^{\mathrm{c}} \displaystyle\int_a^{r_{\mathrm{c}}} \zeta\beta_{\mathrm{M}}(\zeta) J_\lambda\left(\bar{X}_\zeta\right)\mathrm{d}\zeta - J_\lambda^{\mathrm{c}} \int_a^{r_{\mathrm{c}}} \zeta\beta_{\mathrm{M}}(\zeta) Y_\lambda\left(\bar{X}_\zeta\right)\mathrm{d}\zeta \right\} & \text{(a)} \\ I_2^{\mathrm{c}} = \pi\dfrac{\gamma}{\kappa}\left\{ Y_\lambda^{\mathrm{c}} \displaystyle\int_a^{r_{\mathrm{c}}} \zeta\beta_{\mathrm{M}}(\zeta) F_{a,\zeta} J_\lambda\left(\bar{X}_\zeta\right)\mathrm{d}\zeta - J_\lambda^{\mathrm{c}} \int_a^{r_{\mathrm{c}}} \zeta\beta_{\mathrm{M}}(\zeta) F_{a,\zeta} Y_\lambda\left(\bar{X}_\zeta\right)\mathrm{d}\zeta \right\} & \text{(b)} \end{cases} \tag{S5}$$

, with $\gamma = \bar{\kappa}_{\mathrm{a}} / \left(a^2 \varepsilon \bar{K}_{\mathrm{ML}}\right)$ (m^{-2}) and $F_{a,r} = \displaystyle\int_a^r \zeta^{-2}\beta_{\mathrm{M}}^{-1}(\zeta)\mathrm{d}\zeta$ (m^{-1}) similar to the definition given in the main text.

Finally, using Eq. (26) and Eq. (S1c), we obtain

$$1 - c_1 - c_2 F_{a,r_{\mathrm{c}}} + \varepsilon\bar{K}_{\mathrm{ML}} = 0 \tag{S6}$$

The solution of the linear algebraic system consisting of Eqs. (S2), (S3), (S4) and (S6) yields $\alpha_{1,2}$ and $c_{1,2}$. After rearrangements, we obtain for c_2

$$c_2 = \left(1 + \varepsilon\bar{K}_{\mathrm{ML}}\right) F_{a,r_{\mathrm{c}}}^{-1} \frac{1 + U_{\mathrm{a,c}}\varepsilon\bar{K}_{\mathrm{ML}}\nu a^{-1}\left(I_1^{\mathrm{c}} - \dfrac{r_{\mathrm{c}}}{1+\varepsilon\bar{K}_{\mathrm{ML}}}\right)}{1 + U_{\mathrm{a,c}}\varepsilon\bar{K}_{\mathrm{ML}}\nu a^{-1}\left(I_1^{\mathrm{c}} - F_{a,r_{\mathrm{c}}}^{-1} I_2^{\mathrm{c}}\right)} \tag{S7}$$

, where $\nu = \sqrt{z^{-1} z_{\mathrm{M}} \bar{\kappa}_{\mathrm{a}} \left| y_{\mathrm{a}} \right|}$. The term $U_{\mathrm{a,c}}$ in Eq. (S7) is defined by

$$U_{\mathrm{a,c}} = \frac{J_\lambda^{\mathrm{a}}\mathrm{d}Y_\lambda^{\mathrm{a}} - Y_\lambda^{\mathrm{a}}\mathrm{d}J_\lambda^{\mathrm{a}}}{J_\lambda^{\mathrm{a}} Y_\lambda^{\mathrm{c}} - J_\lambda^{\mathrm{c}} Y_\lambda^{\mathrm{a}} + \nu\left(J_\lambda^{\mathrm{c}}\mathrm{d}Y_\lambda^{\mathrm{a}} - Y_\lambda^{\mathrm{c}}\mathrm{d}J_\lambda^{\mathrm{a}}\right)} \tag{S8}$$

, or, equivalently, after substitution of the defining expressions of $\mathrm{d}J_\lambda^{\mathrm{a}}$ and $\mathrm{d}Y_\lambda^{\mathrm{a}}$ into Eq. (S8),

$$U_{\mathrm{a,c}} = \frac{J_\lambda^{\mathrm{a}} Y_{\lambda+1}^{\mathrm{a}} - Y_\lambda^{\mathrm{a}} J_{\lambda+1}^{\mathrm{a}}}{\nu\left(J_\lambda^{\mathrm{c}} Y_{\lambda+1}^{\mathrm{a}} - J_{\lambda+1}^{\mathrm{a}} Y_\lambda^{\mathrm{c}}\right) + \left(1 + \nu\lambda_{\mathrm{a}}\right)\left(J_\lambda^{\mathrm{a}} Y_\lambda^{\mathrm{c}} - J_\lambda^{\mathrm{c}} Y_\lambda^{\mathrm{a}}\right)} \tag{S9}$$

The constant c_1 then follows from Eqs. (S6)-(S7)

$$c_1 = \left(1 + \varepsilon\bar{K}_{\mathrm{ML}}\right) \frac{U_{\mathrm{a,c}}\varepsilon\bar{K}_{\mathrm{ML}}\nu a^{-1}\left(\dfrac{r_{\mathrm{c}}}{1+\varepsilon\bar{K}_{\mathrm{ML}}} - F_{a,r_{\mathrm{c}}}^{-1} I_2^{\mathrm{c}}\right)}{1 + U_{\mathrm{a,c}}\varepsilon\bar{K}_{\mathrm{ML}}\nu a^{-1}\left(I_1^{\mathrm{c}} - F_{a,r_{\mathrm{c}}}^{-1} I_2^{\mathrm{c}}\right)} \tag{S10}$$

, and the expressions of the constants $\alpha_{1,2}$ then read as

$$\begin{cases} \alpha_1 = \dfrac{f_2}{f_1 Y_\lambda^{\mathrm{c}} - f_2 J_\lambda^{\mathrm{c}}}\left[\left(1 + \varepsilon\bar{K}_{\mathrm{ML}}\right)\left(I_1^{\mathrm{c}} - \dfrac{r_{\mathrm{c}}}{1+\varepsilon\bar{K}_{\mathrm{ML}}}\right) + c_2\left(I_2^{\mathrm{c}} - I_1^{\mathrm{c}} F_{a,r_{\mathrm{c}}}\right)\right] & \text{(a)} \\ \alpha_2 = -\dfrac{f_1}{f_1 Y_\lambda^{\mathrm{c}} - f_2 J_\lambda^{\mathrm{c}}}\left[\left(1 + \varepsilon\bar{K}_{\mathrm{ML}}\right)\left(I_1^{\mathrm{c}} - \dfrac{r_{\mathrm{c}}}{1+\varepsilon\bar{K}_{\mathrm{ML}}}\right) + c_2\left(I_2^{\mathrm{c}} - I_1^{\mathrm{c}} F_{a,r_{\mathrm{c}}}\right)\right] & \text{(b)} \end{cases} \tag{S11}$$

, where we defined the scalars $f_{1,2}$ (m^{-1}) according to

$$\begin{cases} f_1 = -a^{-1}\left[a\theta_{\mathrm{a}} \mathrm{d}J_\lambda^{\mathrm{a}} - \beta_{\mathrm{M}}^{\mathrm{a}} \varepsilon \bar{K}_{\mathrm{ML}} J_\lambda^{\mathrm{a}} \right] & \text{(a)} \\ f_2 = -a^{-1}\left[a\theta_{\mathrm{a}} \mathrm{d}Y_\lambda^{\mathrm{a}} - \beta_{\mathrm{M}}^{\mathrm{a}} \varepsilon \bar{K}_{\mathrm{ML}} Y_\lambda^{\mathrm{a}} \right] & \text{(b)} \end{cases} \tag{S12}$$

All the above expressions of $\alpha_{1,2}$ and $c_{1,2}$ involve the non-modified Bessel functions of the first and second type with order λ or $\lambda+1$, specified at the positions $r=a$ and $r=r_{\mathrm{c}}$ or, equivalently, at $\bar{X}_{\mathrm{a}} = \bar{X}_{r=a}$ and $\bar{X}_{\mathrm{c}} = \bar{X}_{r=r_{\mathrm{c}}}$, where $\bar{X}_r$ is given by Eq. (29) in the main text. The evaluation of $J_\lambda\left(\bar{X}_r\right)$ and $Y_\lambda\left(\bar{X}_r\right)$ may be done on the basis of the infinite Taylor series expansion of $J_\lambda\left(\bar{X}_r\right)$ and the functional relationship existing between $J_\lambda\left(\bar{X}_r\right)$ and $Y_\lambda\left(\bar{X}_r\right)$, i.e.

$$\begin{cases} J_\lambda\left(\bar{X}_r\right) = \displaystyle\sum_{\mathrm{M}=0}^{\infty} \frac{(-1)^{\mathrm{M}}\, \bar{X}_{\mathrm{a}}^{\,2\mathrm{M}+\lambda}}{2^{2\mathrm{M}+\lambda}\,\Gamma(1+\lambda+\mathrm{M})\mathrm{M}!} \mathrm{e}^{-(\kappa\mathrm{M}+h)(r-a)} & \text{(a)} \\ Y_\lambda\left(\bar{X}_r\right) = \dfrac{\cos(\lambda\pi) J_\lambda\left(\bar{X}_r\right) - J_{-\lambda}\left(\bar{X}_r\right)}{\sin(\lambda\pi)} & \text{(b)} \end{cases} \tag{S13}$$

, with Γ the Gamma function, and $h = \bar{h}_{\mathrm{a}} / a = \kappa\lambda/2$ (m^{-1}) where $\bar{h}_{\mathrm{a}}$ is defined by Eq. (20). Accordingly, using the relationship $\bar{X}_{\mathrm{c}}^{\,\lambda} = \bar{X}_{\mathrm{a}}^{\,\lambda}\sqrt{1-\alpha}$ with $\alpha = 1 - \mathrm{e}^{2\bar{h}_{\mathrm{a}}(1-r_{\mathrm{c}}/a)}$, and recalling that $\mathrm{e}^{-\kappa(r_{\mathrm{c}}-a)} = 0$ in line with the conditions $1/\kappa << a << r_{\mathrm{c}}$ adopted in this work, we show that Eq. (S13) leads to the following expressions of J_λ^{c}, Y_λ^{c}, J_λ^{a} and Y_λ^{a}

$$\begin{cases} J_\lambda^{\mathrm{c}} = \dfrac{\bar{X}_{\mathrm{a}}^{\,\lambda}}{2^\lambda \Gamma(1+\lambda)}\sqrt{1-\alpha} & \text{(a)} \\ Y_\lambda^{\mathrm{c}} / J_\lambda^{\mathrm{c}} = 1 \Big/ \left[\dfrac{\bar{X}_{\mathrm{a}}^{\,2\lambda}(1-\alpha)}{\chi(\lambda) + \bar{X}_{\mathrm{a}}^{\,2\lambda}(1-\alpha)} \tan(\lambda\pi) \right] & \text{(b)} \\ J_\lambda^{\mathrm{a}} = \bar{X}_{\mathrm{a}}^{\,\lambda}\, j\left(\lambda, \bar{X}_{\mathrm{a}}\right) & \text{(c)} \\ Y_\lambda^{\mathrm{a}} = \bar{X}_{\mathrm{a}}^{\,-\lambda}\, \bar{y}\left(\lambda, \bar{X}_{\mathrm{a}}\right) & \text{(d)} \end{cases} \tag{S14}$$

, where the λ-dependent functions $\chi(\lambda)$, $j\left(\lambda, \bar{X}_{\mathrm{a}}\right)$ and $\bar{y}\left(\lambda, \bar{X}_{\mathrm{a}}\right)$ involved in Eq. (S14) are defined by

$$\begin{cases} \chi(\lambda) = -4^\lambda \lambda \pi^{-1} \Gamma(\lambda)^2 \tan(\lambda\pi) & \text{(a)} \\ j\left(\lambda, \bar{X}_{\mathrm{a}}\right) = \displaystyle\sum_{\mathrm{M}=0}^{\infty} \frac{(-1)^{\mathrm{M}}\, \bar{X}_{\mathrm{a}}^{\,2\mathrm{M}}}{2^{2\mathrm{M}+\lambda}\,\Gamma(1+\lambda+\mathrm{M})\mathrm{M}!} & \text{(b)} \\ \bar{y}\left(\lambda, \bar{X}_{\mathrm{a}}\right) = \dfrac{\cos(\lambda\pi)\bar{X}_{\mathrm{a}}^{\,2\lambda} j\left(\lambda, \bar{X}_{\mathrm{a}}\right) - j\left(-\lambda, \bar{X}_{\mathrm{a}}\right)}{\sin(\lambda\pi)} & \text{(c)} \end{cases} \tag{S15}$$

The integrals I_1^{c} (m) and I_2^{c} (dimensionless) defined by Eq. (S5) and appearing in the expressions of $\alpha_{1,2}$ and $c_{1,2}$ can be evaluated either numerically or after substitution of $J_\lambda\left(\bar{X}_r\right)$ and $Y_\lambda\left(\bar{X}_r\right)$ by Eq. (S13). Adopting the latter method, we can decompose $I_{1,2}^{\mathrm{c}}$ in the forms

$$\begin{cases} I_1^{c} = h^{-1} I_1^{c,y_a \to 0} + \kappa^{-1} I_1^{c,y_a} & \text{(a)} \\ I_2^{c} = \bar{h}_a^{-1} I_2^{c,y_a \to 0} + (\kappa a)^{-1} I_2^{c,y_a} & \text{(b)} \end{cases} \tag{S16}$$

, which makes explicit the contribution of the key length scales h^{-1} and κ^{-1} and that of their dimensionless forms $\bar{h}_a^{-1}$ and $(\kappa a)^{-1}$. In Eq. (S16), $I_{1,2}^{c,y_a \to 0}$ and $I_{1,2}^{c,y_a}$ are dimensionless and refer to the case where there are no electrostatic effects at stake ($y_a \to 0$) and to an electrostatic correction term, respectively. After some algebra, the defining expressions of $I_{1,2}^{c,y_a \to 0}$ and $I_{1,2}^{c,y_a}$ can be recast in the forms

$$\begin{cases} I_1^{c,y_a \to 0} = \dfrac{(2-\alpha)\bar{h}_a + \alpha}{\alpha - 1} \dfrac{\sqrt{1-\alpha}}{2\left(1 + \varepsilon \bar{K}_{ML}\right)} + \dfrac{\bar{h}_a}{1 + \varepsilon \bar{K}_{ML}} \dfrac{r_c}{a} & \text{(a)} \\ I_2^{c,y_a \to 0} = \dfrac{1}{2\left(1 + \varepsilon \bar{K}_{ML}\right)} \left(-\dfrac{\alpha}{\sqrt{1-\alpha}} + 2\bar{h}_a \left(\dfrac{r_c}{a} - 1 \right) \right) & \text{(b)} \end{cases} \tag{S17}$$

and

$$\begin{cases} I_1^{c,y_a} = \left\{ -\sum_{r\_J}(\lambda) \left(1 + \dfrac{1-\alpha}{\chi(\lambda)\cos(\lambda\pi)} \dfrac{\sum_{r\_J}(-\lambda)}{\sum_{r\_J}(\lambda)} \right) + z^{-1} z_M y_a \sum_{r\exp\_J}(\lambda) \left(1 + \dfrac{1-\alpha}{\chi(\lambda)\cos(\lambda\pi)} \dfrac{\sum_{r\exp\_J}(-\lambda)}{\sum_{r\exp\_J}(\lambda)} \right) \right\} \dfrac{2^{\lambda}\Gamma(\lambda)}{\sqrt{1-\alpha}\left(1 + \varepsilon \bar{K}_{ML}\right)} & \text{(a)} \\ I_2^{c,y_a} = -\dfrac{2^{\lambda}\Gamma(\lambda)}{\left(1 + \varepsilon \bar{K}_{ML}\right)} \dfrac{1}{\sqrt{1-\alpha}} \left[\Phi(\lambda) + \dfrac{1-\alpha}{\chi(\lambda)\cos(\lambda\pi)} \Phi(-\lambda) \right] & \text{(b)} \end{cases} \tag{S18}$$

, where the λ-dependent function $\Phi(\lambda)$ involved in Eq. (S18b) is

$$\begin{aligned} \Phi(x) = \sum_{r\_J}(x) \left[1 - \bar{h}_a \frac{\sum_J(x)}{\sum_{r\_J}(x)} \right] + z^{-1} z_M y_a \Bigg\{ \sum_{\exp\_J}(x) \left[\bar{h}_a - \left(1 + \frac{1}{\kappa a} \right) \frac{\sum_{r\exp\_J}(x)}{\sum_{\exp\_J}(x)} \right] + \\ \frac{1}{\kappa a} \left[\sum_{r\_J}(x) + \frac{1 + sign(x)\bar{h}_a - \left(1 + sign(x) h r_c\right)\left(\sqrt{1-\alpha}\right)^{sign(x)}}{2^x \Gamma(1+x)} \right] \Bigg\} \end{aligned} \tag{S19}$$

, with x a dummy variable. The other λ-dependent terms $\sum_J(\lambda)$, $\sum_{\exp\_J}(\lambda)$, $\sum_{r\_J}(\lambda)$ and $\sum_{r\exp\_J}(\lambda)$ involved in Eqs. (S18)-(S19) are the (dimensionless) infinite series we write in the following forms

$$\begin{cases} \sum_J(x) = \sum_{M=1}^{\infty} \dfrac{(-1)^M \bar{X}_a^{2M}}{2^{2M+x}\Gamma(1+x+M)M!} \dfrac{1}{\left(sign(x) + M\kappa/h\right)} & \text{(a)} \\ \sum_{\exp\_J}(x) = \sum_{M=0}^{\infty} \dfrac{(-1)^M \bar{X}_a^{2M}}{2^{2M+x}\Gamma(1+x+M)M!} \dfrac{1}{\left(sign(x) + (1+M)\kappa/h\right)} & \text{(b)} \\ \sum_{r\_J}(x) = \sum_{M=1}^{\infty} \dfrac{(-1)^M \bar{X}_a^{2M}}{2^{2M+x}\Gamma(1+x+M)M!} \dfrac{1 + \left(sign(x) + M\kappa/h\right)\bar{h}_a}{\left(sign(x) + M\kappa/h\right)^2} & \text{(c)} \\ \sum_{r\exp\_J}(x) = \sum_{M=0}^{\infty} \dfrac{(-1)^M \bar{X}_a^{2M}}{2^{2M+x}\Gamma(1+x+M)M!} \dfrac{1 + \left(sign(x) + (1+M)\kappa/h\right)\bar{h}_a}{\left(sign(x) + (1+M)\kappa/h\right)^2} & \text{(d)} \end{cases} \tag{S20}$$

b. Case of (strictly) negative surface potential $y_a < 0$**.** In this situation, Eqs. (S1)-(S20) remain valid after replacing $\bar{X}_{a\le r\le r_c}$ by $-i\bar{X}_{a\le r\le r_c}$ with *i* the imaginary number ($i^2 = -1$). Alternatively, solutions of the M and ML concentration profiles for $y_a < 0$ may be expressed in terms of the modified Bessel functions of the first and second type with order λ in place of the non-modified Bessel functions adopted for the case $y_a > 0$.

c. Comments. The demonstrations of all analytical expressions reported above were carefully checked with the help of Mathcad Prime 8.0 calculus environment that we further used as help to generate the analytical results given in **Figures 3C-3D** (colored dotted lines therein). In particular, starting from Eq. (30) in the main text, additional expressions may be developed for the lability index ξ (Eq. (30)) after substitution of Eqs. (S11)-(S12) and Eqs. (S14)-(S20). The results give rise to cumbersome expressions for ξ (not shown here) that however find their utility in minimizing the instabilities connected to the inherent singularities of the non-modified Bessel functions invoked in the main text (§2.2.3).

II. Supplementary Figures.

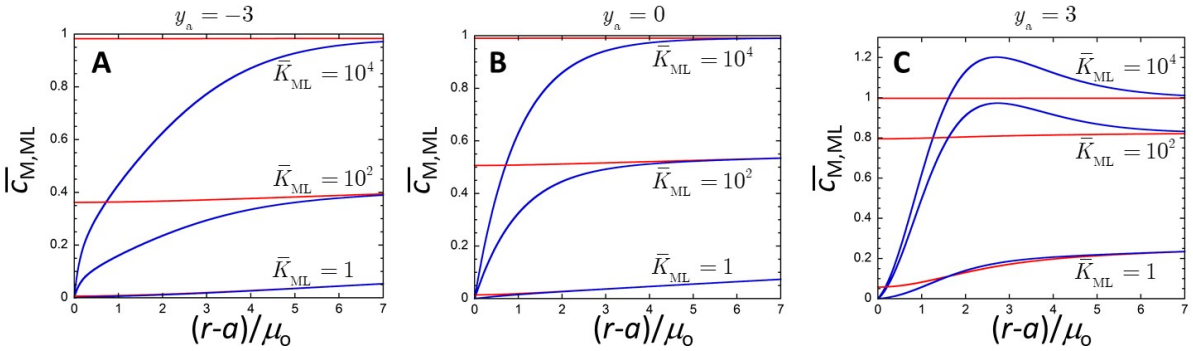

Figure S1. Spatial distributions of the concentration profiles $\bar{c}_M(r) = c_M(r)/c_M^*$ (blue) and $\bar{c}_{ML}(r) = c_{ML}(r)/c_{ML}^*$ (red) for y_a = -3 (**A**), 0 (**B**) and 3 (**C**) and different $\bar{K}_{ML}$ (indicated). Adopted model parameters are $1/\kappa = 10$ nm, $a = 1$ μm, $r_c/a = 50$, $\varepsilon = 1$, $z_M = 2$, $z_{ML} = z_L = 0$, $\kappa\mu_o = 1$.

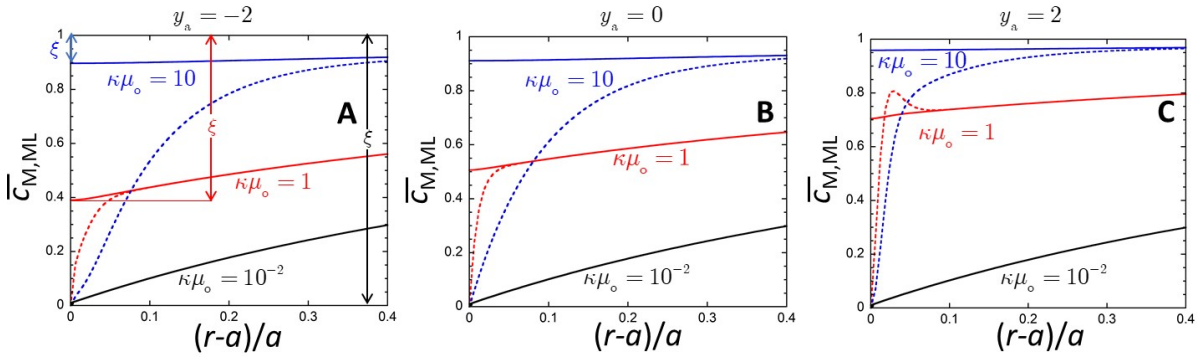

Figure S2. Spatial distributions of the concentration profiles $\bar{c}_M(r) = c_M(r)/c_M^*$ (dotted lines) and $\bar{c}_{ML}(r) = c_{ML}(r)/c_{ML}^*$ (solid lines) for y_a = -2 (**A**), 0 (**B**) and 2 (**C**) plotted as a function of the scaled space variable $(r-a)/a$ for $\kappa\mu_o = 10$ (blue), 1 (red) and 10^{-2} (black). Dotted and solid black curves for $\bar{c}_M(r)$ and $\bar{c}_{ML}(r)$, respectively, are coincident for $\kappa\mu_o = 10^{-2}$ (this is the fully labile limit, $\xi \to 1$). Adopted model parameters are $1/\kappa = 10$ nm, $a = 1$ μm, $r_c/a = 50$, $\varepsilon = 1$, $\bar{K}_{ML} = 10^2$, $z_M = 2$, $z_{ML} = z_L = 0$. The definition of ML lability index ξ (Eq. (14)) is illustrated graphically in panel (**A**) for the three $\kappa\mu_o$ conditions examined.

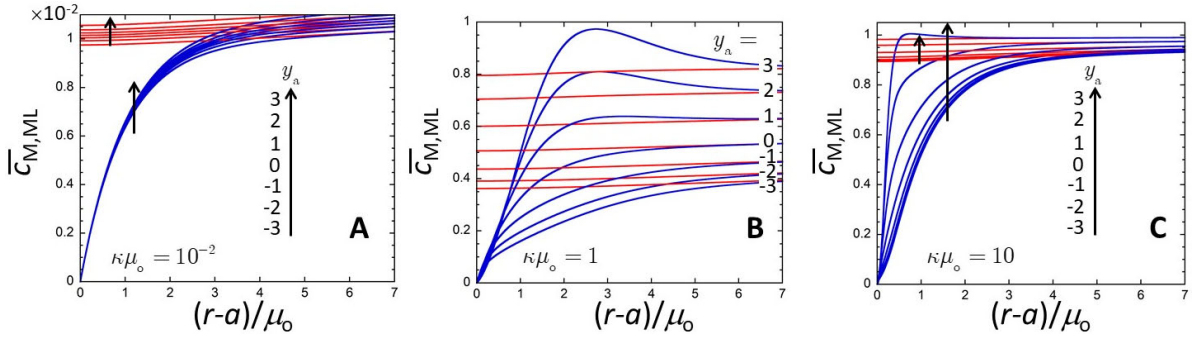

Figure S3. Spatial distributions of the concentration profiles $\bar{c}_M(r) = c_M(r)/c_M^*$ (blue) and $\bar{c}_{ML}(r) = c_{ML}(r)/c_{ML}^*$ (red) at various values of y_a (indicated) and plotted as a function of the scaled space variable $(r-a)/\mu_o$ for $\kappa\mu_o = 10^{-2}$ (**A**), 1 (**B**) and 10 (**C**). Adopted model parameters are $1/\kappa = 10$ nm, $a = 1$ μm, $r_c/a = 50$, $\varepsilon = 1$, $\bar{K}_{ML} = 10^2$, $z_M = 2$, $z_{ML} = z_L = 0$. Note the $\times 10^{-2}$ scaling factor in the y-axis of panel (**A**).

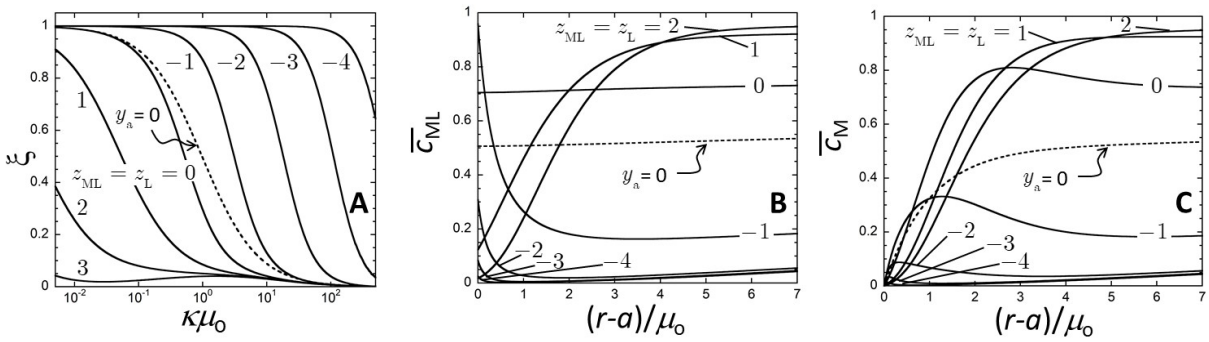

Figure S4. Dependence of ξ on $z_{ML} = z_L$ (indicated) as a function of $\kappa\mu_o$ (**A**). Corresponding $\bar{c}_{ML}(r)$ (**B**) and $\bar{c}_M(r)$ (**C**) profiles for $\kappa\mu_o = 1$. Adopted model parameters are $1/\kappa = 10$ nm, $y_a = 2$, $a = 1$ μm, $r_c/a = 50$, $\varepsilon = 1$, $\bar{K}_{ML} = 10^2$, $z_M = 2$. The dotted lines specify in **(A)**, **(B)** and **(C)** the situation for uncharged particles ($y_a = 0$).